Role of inelastic couplings in the ^{4}He + ^{208}Pb elastic scattering in a wide energy range

Role of inelastic couplings in the ^{4}He + ^{208}Pb elastic scattering in a wide energy range.

L. C. Chamon, L. R. Gasques and J. C. Zamora.

Universidade de Sao Paulo, Instituto de Fisica, Rua do Matao, 1371, 05508-090, Sao Paulo, SP, Brazil.

E-mail: lchamon@if.usp.br

Abstract. The phenomenological strengths of the real part of the optical potential, obtained from elastic scattering data analyses within the optical model approach, present significant energy-dependence. This behavior has been associated to the intrinsic energy-dependence of the effective nucleon-nucleon interaction. However, in earlier works, we proposed that at least part of this dependence can arise from the effect of couplings to inelastic states of the nuclei. In order to deepen this study, in this paper we present extensive data analyses for the elastic scattering and inelastic excitation of 111 states of ^{208}Pb, for the ^{4}He + ^{208}Pb system in a wide energy range. With the purpose of comparison, the theoretical cross sections are obtained in different approaches for the imaginary part of the potential, and within both contexts: optical model (distorted wave Born approximation) and coupled-channel calculations.

Submitted to: *J. Phys. G: Nucl. Phys.*

1. Introduction

With regard to nuclear reactions, the optical model (OM) is the simplest theoretical approach to study the elastic scattering process and has been extensively used in data analyses for many systems over a wide energy range. The strengths of the real part of the phenomenological optical potentials (OP) that fit the data have an important energy dependence. For energies around the barrier height, the energy dependence of the OP is related to the closure of the reaction channels and the corresponding behavior is known as threshold anomaly [1]. The OP energy dependence has also been observed in a much wider energy range and, in this case, it is associated to the effective nucleon-nucleon interaction (see *e.g.* [2–4]). However, this concept has been questioned in recent studies, in which a significant part of the OP energy dependence is related to the effects of couplings to inelastic states [5–7]. The purpose of the present work is to deepen this study.

Due to numerical convergence and computing time problems, solving coupled equations involving a large number of excited states, including several states at very

high excitation energies, is a quite difficult task. In [7], we developed a new method that greatly improves the convergence and computing time of such calculations. This method is used in the present work to perform large scale coupled-channel (CC) calculations for ^{4}He + ^{208}Pb. The choice of this system for the present paper is for two reasons: it was the test case of the method developed in [7], and also because large amount of data for the inelastic excitation of ^{208}Pb is available in the literature .

Within the OM, the real and imaginary parts of the OP involve contributions related to the couplings of the elastic process with the reaction channels. In principle, if all important peripheral channels are explicitly included in the CC calculations, the absorption of flux by the fusion process could be simulated through an imaginary part restricted to an inner region of distances smaller than the barrier radius. This hypothesis has been assumed in many works. Nevertheless, in most of these papers the number of peripheral channels included in the calculations is not very large. In the present work, we intend to show that important part of the polarization can arise from the joint contribution of many states with high excitation energies that individually are not significant.

In order to investigate the effects of the inelastic couplings on the elastic scattering cross sections, we compare the results obtained through CC calculations with those from the distorted wave Born approximation (DWBA). We include explicitly more than one hundred inelastic states in the coupling scheme. In our calculations, we assume two models for the imaginary part of the OP. In the first model, the OP imaginary part simulates the fusion process through a Woods-Saxon (WS) shape with parameters values fixed to provide only internal absorption. With this model, we study the capability and also the limitations of describing the data (elastic and inelastic) as a function of the energy without surface absorption arising from the OP. The model works very well for low energies but it fails progressively with the increasing of energy. In fact, at high energies other peripheral channels, beyond those included in the CC scheme, become significant and require superficial absorption. In the second model for the imaginary part of the OP, we add another term to the WS which is proportional to the real part. This second term provides superficial absorption that can be varied through an adjustable normalization factor. The value of this factor is adjusted to fit the elastic scattering cross sections. With this, we study the variation of the superficial absorption due to the inelastic couplings as a function of the energy by comparing results of the CC and DWBA calculations. The data set analysed here is quite wide, containing cross section data for elastic scattering and more than one hundred of inelastic states, in energies ranging from the sub-coulomb region to $E_{Lab} = 699$ MeV. With this we study in detail the characteristics of the reaction mechanisms as a function of the energy.

2. The Coupling Scheme

We adopt a parameter-free model for the real part of the OP: the recently proposed Brazilian Nuclear potential (BNP) [8]. The effective interaction assumed in the context

of the BNP was firmly based on data analyses for alpha-nucleus systems [5, 9, 10] and, therefore, we consider the BNP an appropriated choice for the nuclear interaction in the present study. In the corresponding `REGINA` code [8], we assumed the option of "experimental" charge and matter densities for ^{4}He and theoretical Dirac-Hartree-Bogoliubov (DHB) distributions for ^{208}Pb. The corresponding root-mean-square radii for the ^{208}Pb charge and matter densities are: 5.53 fm and 5.64 fm, respectively. A fit of the ^{208}Pb charge density through a Woods-Saxon (WS) shape provides the following corresponding values: $\rho_0 = 0.0624$ fm^{-3}, $R_0 = 6.65$ fm and $a = 0.55$ fm. The same procedure for the matter density provides: $\rho_0 = 0.1550$ fm^{-3}, $R_0 = 6.67$ fm and $a = 0.60$ fm.

In the present work, we study couplings to inelastic processes involving the excitation of a large number of ^{208}Pb states. In our approach, the absorption of flux by other reaction channels is simulated through the imaginary part included in the OP. ^{4}He is considered a quite inert nucleus and, therefore, the transfer reactions for ^{4}He + ^{208}Pb should not be important, mainly at energies around the Coulomb barrier. Thus, in this low energy region, the OP imaginary part would be mostly related to fusion, therefore restricted to the innermost spatial region. In other energy regions, where contributions of peripheral reactions (aside those of inelastic couplings) can become important, the use of an OP imaginary part with superficial absorption should be appropriated.

Thus, we assume the sum of two contributions for the imaginary part of the OP: one with a WS shape and other proportional to the real part

$$W(R) = \frac{-W_0}{1 + \exp\left[(R - R_{I0})/a_i\right]} + N_I\, V_{BNP}(R). \qquad (1)$$

The parameter values for the WS part are fix and established to provide only internal absorption (see [5]): $W_0 = 60$ MeV, $R_{I0} = 6$ fm, $a_i = 0.25$ fm. N_I is an adjustable parameter to fit the elastic scattering data. This latter contribution of $W(R)$ is used only in cases where, in addition to fusion, it is necessary to simulate some absorption of flux by the peripheral reaction channels. Even so, in some of these cases the fit to the elastic scattering data can still result in vanishing surface absorption ($N_I = 0$), a situation in which the fixed WS part of $W(R)$ guarantees internal absorption simulating fusion. It is important to mention that the $N_I\, V_{BNP}$ term in eq. (1) also provides internal absorption when N_I is not too small (at $R = 0$ we have $V_{BNP} \approx -255$ MeV). In these cases, the WS part of the imaginary potential is irrelevant in the sense that calculations including or not this term in the OP result in the same cross sections for the elastic and inelastic channels.

The coupling scheme involves a very large number of ^{208}Pb states, many of them with quite high excitation energies. As already mentioned, we adopt the efficient method proposed in [7] to solve the coupled equations. In order to use this method, it is required to treat the couplings in first order, *i.e.* the inelastic states are directly coupled to the elastic channel (there are no couplings among the inelastic states). We label with S the spin of a particular ^{208}Pb state. For each total angular momentum J, there are at most

$S+1$ coupled equations associated to this state, with coupling potentials given by:

$$V_N(R) = \frac{i^{L-J}}{\sqrt{4\pi}} C^{J\,S\,L}_{0\,0\,0} \left[\delta_C \, Z_1 Z_2 e^2 \left\langle r^{S-1} \right\rangle \frac{S+2}{2S+1} V_C(R) - \delta_N \frac{\partial V_{BNP}(R)}{\partial R} - i\delta_W \frac{\partial W(R)}{\partial R} \right] \quad (2)$$

$$V_C(R) = \begin{cases} \frac{1}{R^{S+1}} \text{ for } R \geq R_C \\ \\ \frac{R^S}{R_C^{2S+1}} \text{ for } R \leq R_C \end{cases} \quad (3)$$

where L is the orbital angular momentum, δ_N, δ_W and δ_C are the respective nuclear (real and imaginary parts) and Coulomb deformation lengths for this state. According to the WS ^{208}Pb charge density, we assumed $R_C = R_0 = 6.65$ fm in eq. (3). The Clebsch-Gordan coefficients in eq. (2) guarantee the angular momentum conservation. The moments $\left\langle r^{S-1} \right\rangle$ are calculated through the ^{208}Pb charge density. Table 1 provides the respective values of $\sqrt[L]{\langle r^L \rangle}$. We have not included Coulomb contributions in the couplings for $S = 0$ and $S = 1$, assuming $\delta_C = 0$ in these cases.

Table 1. Values of $\sqrt[L]{\langle r^L \rangle}$ for the charge density of ^{208}Pb.

L	1	2	3	4	5	6	7	8	9
$\sqrt[L]{\langle r^L \rangle}$ (fm)	5.30	5.53	5.71	5.88	6.03	6.16	6.29	6.41	6.53

In this approach, the transition probability for Coulomb excitation can be obtained from:

$$B(E\lambda) \uparrow = e^2 \left| \frac{\delta_C Z (\lambda+2) \left\langle r^{\lambda-1} \right\rangle}{4\pi} \right|^2, \quad (4)$$

where δ_C is the Coulomb deformation length. $B(E\lambda) \uparrow$ can also be defined for nuclear excitation by exchanging δ_C with δ_N and Z with A in this equation.

In some works, it is claimed that different form factors should be assumed for the monopole and dipole (see *e.g.* [11]) because they are couplings of second-order. Thus, we have also used the following nuclear couplings for $S = 0$:

$$V_N(R) = -i^{L-J} \frac{\delta_N}{R_0\sqrt{4\pi}} C^{J\,S\,L}_{0\,0\,0} \left[3 + R\frac{\partial}{\partial R} \right] U_{OP}(R), \quad (5)$$

and for $S = 1$:

$$V_N(R) = -i^{L-J} \frac{\delta_N}{R_0^2\sqrt{4\pi}} C^{J\,S\,L}_{0\,0\,0} \left[10R + \left(3R^2 - \frac{5}{3}\left\langle r^2 \right\rangle \right) \frac{\partial}{\partial R} + \epsilon \left(R\frac{\partial^2}{\partial R^2} + 4\frac{\partial}{\partial R} \right) \right] U_{OP}(R), \quad (6)$$

where $U_{OP}(R) = V_{BNP}(R) + i\,W(R)$ is the central OP, $\langle r^2 \rangle = 5.64^2$ fm^2 as a result of the matter density and $\epsilon \approx 0.05$ fm^2 (for ^{208}Pb). However, from the theoretical point of

view, the use of second-order form factors coupling the elastic channel to a particular state should be complemented with couplings in two steps involving two inelastic states besides the fundamental one. For instance, within the vibrational model, the 0_2^+ state of the triplet is coupled to the 0_1^+ fundamental state in one step with a second-order term in deformation, while these same states are coupled in two steps, each one with a first-order term in deformation, through the $0_1^+ \rightarrow 2_1^+ \rightarrow 0_2^+$ path [12]. Two first-order steps are equivalent to one second-order step, and therefore both couplings are equally important to connect the 0_1^+ and 0_2^+ states. Curiously, this complement is not usually considered in works that assume eqs. (5) and (6) in the calculations. Since here we neglect the couplings among inelastic states, the use of the second-order form factors corresponding to eqs. (5) and (6) should not be more "fundamental" than using that of eq. (2). Even so, in this work it will be discussed the effect of assuming both models for the $S = 0$ and $S = 1$ couplings.

The aim of the present work is to study the effect of a large number of inelastic couplings on the elastic scattering. Thus, we use the fairly simple scheme presented here to treat the couplings, since a more fundamental approach such as using transition densities to calculate coupling potentials [12] is impractical when considering many states, including several states with very high excitation energies. On the other hand, the deformation parameter values assumed here were obtained from inelastic scattering data fits and, in this sense, the respective couplings can be considered quite realistic.

Eq. (2) shows that the nuclear coupling involves the deformation of the real and imaginary parts of the OP. Many works also make use of this assumption, but others associate only the real part of the OP in the deformation involved in the inelastic couplings. This subject was already studied earlier as, for example, in [59–62]. Even so, here we provide additional analysis of this question, investigating its characteristics in different energy regions. With this purpose, two parameters δ_N and δ_W are included in the nuclear coupling of eq. (2). However, we assume $\delta_N = \delta_W$ in all calculations, except those in which we test the effect of the deformation of the imaginary part of the OP. Thus, for now on, when we do not mention the δ_W value, it is implicit that $\delta_W = \delta_N$.

In [7] we showed that the effect of the couplings to a set of many inelastic states on the elastic scattering cross section can, in some cases, be simulated through the coupling to only one state. The values of the corresponding deformation length parameters and excitation energies are related by the following expressions:

$$\delta = \sqrt{\sum_{i=1}^{N} \delta_i^2}, \tag{7}$$

$$E^* = \frac{1}{\delta_N^2} \sum_{i=1}^{N} E_i^* \delta_i^2, \tag{8}$$

where N is the number of states of the set of states and δ and E^* are the parameter values of the single state that simulates the effects of the complete set. This correspondence can be used to significantly decrease the number of states considered in CC calculations

and, therefore, it is quite useful. However, in [7] we studied this correspondence only at $E_{\rm Lab} = 139$ MeV. In the present paper, we study the limits of application of this kind of simulation in different energy regions.

3. The Data Set

The height of the s-wave barrier for ^{4}He + ^{208}Pb obtained with the BNP is $V_B = 20.60$ MeV in the center of mass frame (21.00 MeV at the laboratory). We have analysed elastic and inelastic scattering data for this system from $E_{\rm Lab} = 14$ MeV to 699 MeV. The data were obtained in [13–46]. In addition, we assumed deformation parameter values obtained in several works from inelastic scattering data fits for proton + ^{208}Pb [47–56]. The energy spectra of [57, 58] were also included in the data set.

The data analyses (discussed in the following sections) provided the nuclear deformation length values for 111 ^{208}Pb states, which are presented in table 2. Some of these states correspond to giant resonances that can be represented by more than one state. Different works have reported values slightly different for the mean excitation energies of these giant resonances. Here we assume averages of these values. The accurate determination of the δ_C parameter value is not simple when inelastic data at near-barrier energies and forward angles are not available for analyses. Thus, we assumed $\delta_C = \delta_N$ for all states, except for the first 3^- $E^* = 2.615$ MeV one, for which we obtained $\delta_C = 0.797$ fm and $\delta_N = 0.865$ fm. For most states presented in table 2, the deformation length values provided here are compatible with those reported in the original works where the inelastic scattering data were published.

We have analysed experimental elastic scattering angular distributions for the energies presented in table 3. The table also provides the ratio of the relative velocity between the nuclei to the speed of light, v/c. As an estimate for the "size" of a possible relativistic effect, that is not considered in our theoretical calculations, the table also provides the percentage value of the length contraction relative to the proper length, calculated as:

$$C = \left(1 - \sqrt{1 - \frac{v^2}{c^2}}\right) \times 100\%. \quad (9)$$

The contraction reaches about 16% for the highest energy studied here indicating that a non-negligible effect of relativity is expected in the data analyses for the region of high energies.

As already mentioned, the strengths of the real part of the phenomenological OP that fit the elastic scattering data within the OM have an energy dependence. Within the context of the São Paulo potential (SPP) [4], this energy dependence is related to the relative velocity between the nuclei as follows:

$$V_{SPP}(R) \approx V_F(R)\, e^{-4v^2/c^2}, \quad (10)$$

where $V_F(R)$ is an energy independent folding potential. In order to provide an estimate of this effect, table 3 also presents the values of the term e^{-4v^2/c^2}. The effect is negligible

Table 2. Excitation energy (in MeV), spin and nuclear deformation parameter (in fm) values obtained in our analyses for 111 ^{208}Pb states.

E^*	S	δ_N	E^*	S	δ_N	E^*	S	δ_N	E^*	S	δ_N
2.615	3	0.865	4.937	3	0.110	5.774	4	0.060	6.736	3	0.051
3.198	5	0.360	4.952	4	0.092	5.796	4	0.060	6.843	8	0.150
3.708	5	0.220	4.974	3	0.150	5.813	4	0.200	6.925	4	0.140
3.961	5	0.120	4.983	6	0.150	5.874	3	0.080	6.940	3	0.061
4.037	7	0.190	5.010	9	0.120	5.890	8	0.110	7.019	3	0.150
4.054	3	0.090	5.038	3	0.090	5.966	9	0.190	7.060	4	0.110
4.086	2	0.360	5.074	5	0.115	5.993	5	0.198	7.063	1	0.170
4.106	3	0.069	5.085	7	0.043	6.010	3	0.200	7.171	3	0.050
4.141	2	0.058	5.126	2	0.075	6.052	4	0.120	7.114	3	0.140
4.159	2	0.046	5.195	3	0.110	6.089	3	0.067	7.192	4	0.150
4.181	5	0.120	5.210	4	0.140	6.170	2	0.049	7.280	1	0.100
4.240	5	0.130	5.245	3	0.140	6.191	3	0.140	7.302	5	0.120
4.297	5	0.120	5.277	3	0.090	6.233	4	0.150	7.320	2	0.080
4.324	4	0.420	5.292	1	0.190	6.248	7	0.240	7.334	3	0.120
4.403	3	0.058	5.321	3	0.067	6.276	3	0.130	7.382	4	0.186
4.424	6	0.400	5.347	3	0.200	6.314	3	0.100	7.455	2	0.080
4.444	5	0.062	5.378	5	0.110	6.332	6	0.170	7.491	2	0.080
4.463	2	0.039	5.417	7	0.110	6.351	4	0.100	7.517	3	0.100
4.481	6	0.080	5.482	5	0.240	6.381	7	0.140	8.340	4	0.170
4.611	8	0.240	5.517	3	0.300	6.396	4	0.110	9.300	3	0.260
4.680	9	0.110	5.543	7	0.157	6.428	4	0.100	10.800	2	0.600
4.698	3	0.210	5.561	2	0.120	6.445	3	0.080	10.800	4	0.400
4.762	7	0.100	5.659	5	0.150	6.484	1	0.066	12.600	4	0.346
4.842	1	0.170	5.673	3	0.110	6.529	5	0.180	13.700	0	0.440
4.861	8	0.084	5.690	4	0.210	6.615	3	0.160	16.000	6	0.326
4.895	10	0.130	5.721	7	0.120	6.658	4	0.150	18.800	3	0.606
4.923	2	0.050	5.743	9	0.130	6.688	5	0.290	22.000	1	0.512
4.933	4	0.170	5.763	6	0.090	6.704	3	0.100			

($e^{-4v^2/c^2} \approx 1$) in the region around the barrier height, but it becomes more significant as the energy increases reaching the value of 0.31 at $E_{\rm Lab} = 699$ MeV. The potential assumed here (BNP) is energy independent and, therefore, we test the extent to which an energy-independent interaction can describe the data in such a wide region of energies.

Table 3. The table presents the values of bombarding energies, ratio of the relative velocity between the nuclei to the speed of light, the percentage variation of the contraction of the space and the attenuation factor of the São Paulo potential. The table also presents the N_I values obtained from elastic scattering data fits in these energies, in the context of different approaches adopted in the theoretical calculations, and the respective χ^2 values. In the last column, we present the ratio between the N_I values of the CCsup and DWBAsup approaches: CCsup/DWBAsup. Due to ambiguities, this ratio is not presented for some energies (see text for details).

$E_{\rm Lab}$	v/c	C (%)	e^{-4v^2/c^2}	DWBAint	DWBAsup		CCint	CCsup		ratio
				$\chi^2(\%)$	N_I	$\chi^2(\%)$	$\chi^2(\%)$	N_I	χ^2	
17.5	0.10	0.5	0.96	0.5	0	0.5	0.5	0	0.5	-
18.0	0.10	0.5	0.96	0.4	0	0.4	0.5	0	0.5	-
19.0	0.10	0.5	0.96	0.9	0.11	0.6	0.7	0.07	0.6	0.64
20.0	0.10	0.5	0.96	1.0	0.05	0.9	1.0	0.03	1.0	0.60
22.0	0.11	0.6	0.95	5.8	0.23	3.8	1.6	0	1.6	0.00
23.6	0.11	0.6	0.95	15	0.70	3.7	4.7	0.30	2.8	0.43
27.6	0.12	0.7	0.94	49	0.87	5.0	14	0.27	3.0	0.31
40.4	0.15	1.1	0.92	51	0.57	12	18	0.08	8.3	0.14
50.0	0.16	1.3	0.90	30	0.39	13	15	0.13	14	0.33
58.0	0.17	1.5	0.89	69	0.54	11	36	0.19	20	0.35
79.1	0.20	2.1	0.85	74	0.70	17	50	0.35	30	0.50
104	0.23	2.7	0.81	109	0.63	29	77	0.42	37	0.67
120	0.25	3.1	0.78	47	0.61	9.7	32	0.39	12	0.64
139	0.27	3.6	0.75	152	0.61	37	118	0.47	36	0.77
172	0.29	4.4	0.71	51	0.81	13	36	0.52	16	0.64
288	0.37	7.2	0.57	141	5.50	31	111	0.67	47	-
340	0.40	8.4	0.53	141	3.94	44	126	0.80	58	-
386	0.42	9.4	0.49	145	3.00	66	126	0.84	81	-
480	0.46	11.4	0.42	167	2.15	74	130	1.35	83	0.63
699	0.54	15.8	0.31	146	2.31	87	134	1.90	92	0.82

4. Data analyses

In order to illustrate different aspects of our analyses, we performed calculations of cross sections in four different approaches. To facilitate the reader, we adopt different labels for these calculations. We name as DWBAint the OM calculations without couplings (through DWBA) assuming the internal WS imaginary potential (*i.e.* making $N_I = 0$ in eq. (1)). DWBAsup also represents calculations without couplings, but in this case N_I is adjusted to fit the elastic scattering data. CCint and CCsup represent CC calculations including all 111 states of table 2, assuming only the internal WS ($N_I = 0$) or adjusting the N_I value of the superficial potential, respectively.

The data set was obtained from the EXFOR database [63] and also from tables and figures presented in the manuscripts of the references. Thus, we do not know the error bars for part of the data that we have analysed. With the purpose of estimating the quality of the adjust between the theoretical and experimental angular distributions, we define a "chi-square" given by the average percentage difference between experimental ($\sigma_{\rm exp}$) and theoretical ($\sigma_{\rm theo}$) cross sections:

$$\chi^2 = \left(\frac{1}{N}\sum_{i=1}^{N}\frac{\Delta\sigma}{\langle\sigma\rangle}\right)\times 100\%,\ \Delta\sigma = \left|\sigma_{\rm theo}-\sigma_{\rm exp}\right|,\ \langle\sigma\rangle = \frac{\sigma_{\rm theo}+\sigma_{\rm exp}}{2}, \quad (11)$$

where N is the number of data points of the angular distribution. With this definition, the range of variation of chi-square is $0 \leq \chi^2 \leq 200\%$, where a perfect match between data and theoretical cross sections is given by $\chi^2 = 0\%$, while complete disagreement provides $\chi^2 = 200\%$

In table 3, we present the N_I and χ^2 values obtained from the analyses of the elastic scattering angular distributions in different energies. These values were obtained within the DWBAint, DWBAsup, CCint and CCsup approaches. Fig. 1 shows the behavior of the N_I values as a function of the energy in the cases of DWBAsup and CCsup. Note the change from linear scale in the left side of the figure to logarithmic scale (both axes) in the right side. The "error bars" represent N_I regions in which the chi-square varies of 10%, *i.e.* $\chi^2 \leq (1+10\%)\chi^2_{\rm min}$ where $\chi^2_{\rm min}$ is the minimum chi-square value. Therefore, these error bars should not be associated to uncertainties of the N_I values; they just illustrate the sensitivity of the data fits to variations of the N_I value. The lines in the figure represent linear fits to the data, in which only points with $E_{\rm Lab} > V_B = 21$ MeV were considered. For some high energies, there are two N_I regions of local chi-square minimums (in these cases, only the N_I value corresponding to the smallest chi-square is provided in table 3).

The approach without couplings and with internal imaginary potential, DWBAint, provides good precision ($\chi^2 < 1\%$, see table 3) at sub-Coulomb energies ($E_{\rm Lab} < 21$ MeV), but the data description becomes much worse for higher energies. This behavior is expected since the absorption of flux by the peripheral reactions increases with the energy. In fact, the N_I parameter values obtained with surface absorption, within DWBAsup, increase from $N_I \approx 0.1$ in the vicinity of the barrier to $N_I \geq 1$ for the highest energies, and the corresponding χ^2 values are much better than those for DWBAint (mainly for energies above the barrier).

The approach with internal imaginary potential, but now considering the couplings of table 2, CCint, provides much better data description than the DWBAint (compare the respective χ^2 values in table 3). The CCint does not contain any adjustable parameter related to the OP and even so it provides precision (χ^2) better than 20% for the region of energies $E_{\rm Lab} \leq 50$ MeV. This behavior already shows the great importance of the couplings to inelastic states for the elastic scattering process. Nevertheless, the CCint does not work so well for higher energies, probably because further reaction channels besides those of table 2 become important in this energy region. In fact, the

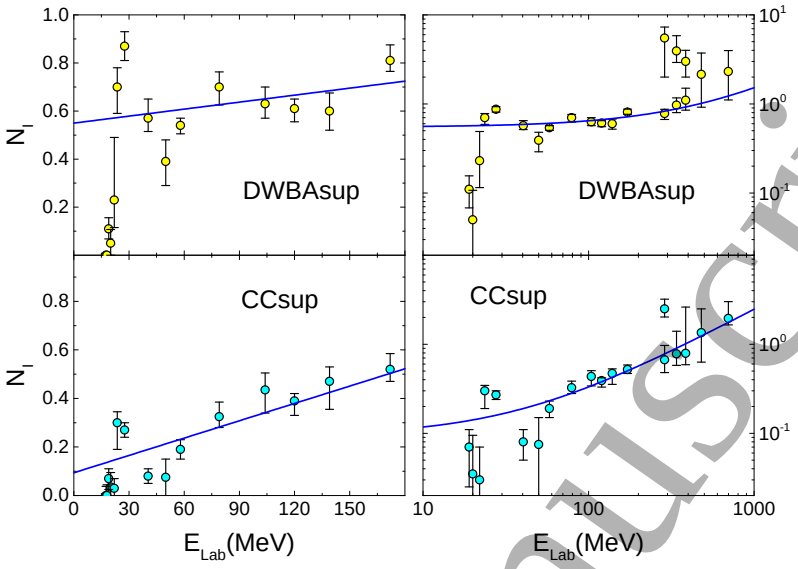

Figure 1. (color online) N_I values as a function of the bombarding energy obtained from elastic scattering data fits within the DWBAsup and CCsup approaches. Note the change from linear scale in the left side of the figure to logarithmic scale (both axes) in the right side. The lines in the figure represent linear fits obtained considering only points with $E_{\rm Lab} > V_B$.

CCsup approach, with superficial imaginary potential, provides increasing N_I values as a function of the energy (see Fig. 1), and significantly better χ^2 values than those from CCint (see table 3).

The last column of table 3 provides the ratio between the N_I values obtained within CCsup and DWBAsup. Due to the corresponding ambiguities, this ratio is not provided for three high energies where two N_I regions of local chi-square minimums were found. All the ratio values are smaller than 1 indicating that the CCsup approach demands less absorption from the OP imaginary part than the DWBAsup. This is expected since the imaginary potential in DWBAsup simulates the absorption of flux of all peripheral reaction channels, while in the CCsup it does not contain the contribution of the 111 inelastic states of table 2 (since they are explicitly considered in the couplings of the CC calculations). For energies below the barrier (that corresponds to $E_{\rm Lab} \leq 21$ MeV) the N_I values are quite small for both CCsup and DWBAsup. For the region of low energies given by $22 \leq E_{\rm Lab} \leq 58$ MeV, the ratio (CCsup/DWBAsup) values are about 0.3 indicating that the couplings included in CCsup are responsible by about 70% of the total superficial absorption of DWBAsup. For higher energies the ratio reaches larger values around 0.7 indicating that the contribution of the 111 inelastic states is less important, probably because in this region more reaction channels are contributing significantly to the total absorption. Note in addition in Fig. 1, that the behavior of the N_I values as a function of the energy in the case of CCsup is smoother than that for DWBAsup, mainly at the region around the barrier: $E_{\rm Lab} \approx V_B = 21$ MeV. This difference is thus related to the effect of the couplings to the inelastic states of table 2.

Now we provide a detailed study of the characteristics of the elastic and inelastic

scattering in different energies.

4.1. Sub-Coulomb energy region: $E_{\rm Lab} \leq 21$ MeV.

In Fig. 2, we show elastic scattering angular distributions for four energies. Data obtained in different references are represented by different symbols. For the purpose of comparison, thin dashed black lines that correspond to $\frac{\sigma_{El.}}{\sigma_{Ruth.}} = 1$ are included in the figure. There is some discrepancy between different data sets, mainly for $E_{\rm Lab} = 17.5$, 18 and 19 MeV at backward angles. The dashed red and dashed-dotted black lines represent the results of theoretical calculations within two different approaches: DWBAint and CCint, respectively. The comparison between these theoretical angular distributions clearly shows that the effect of the couplings on the elastic scattering cross sections is quite small. The N_I values obtained within the DWBAsup in these energies are very small (see table 3), while, as expected, those from CCsup are even closer to zero. The theoretical distributions presented in Fig. 2 are in good agreement with the data for all energies, corroborating that there is no need for including a superficial contribution in the imaginary part of the OP in this low energy region.

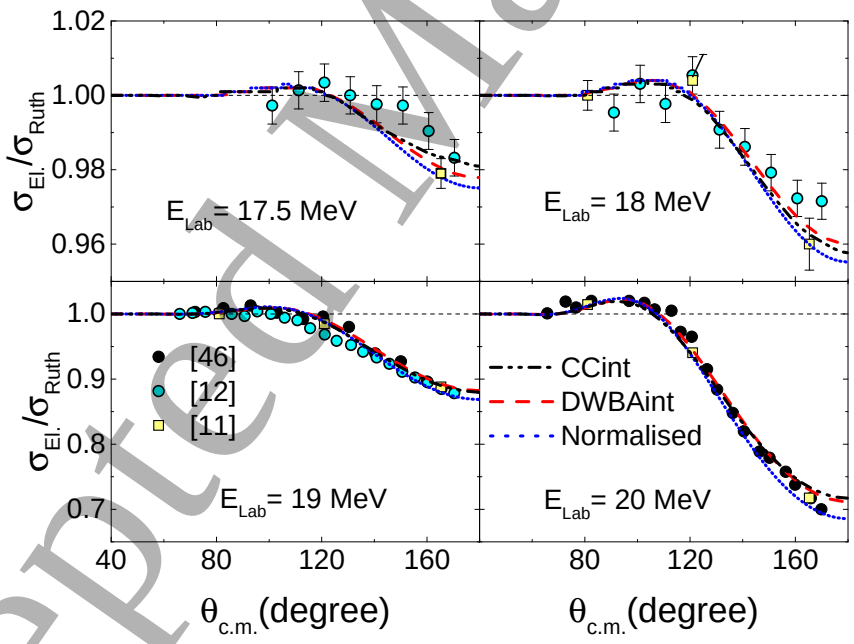

Figure 2. (color online) Experimental angular distributions for the elastic scattering process in different energies. The references where the data were obtained are indicated in the figure. The dashed-dotted black and (thick) dashed red lines represent the results of the CCint and DWBAint approaches, respectively. The dotted blue lines correspond to DWBAint calculations where the real part of the OP was increased by 10%.

In order to investigate the sensitivity of the elastic scattering cross sections to the real part of the OP, we have performed additional DWBAint calculations where the real part was normalised by a factor of 1.1 (10% of variation). The corresponding results are shown as dotted blue lines in Fig. 2. Note that, except for $E_{\rm Lab} = 17.5$ MeV, the effect of varying the normalization by 10% is more significant than that from the couplings.

Another important point: the results corresponding to $E_{\rm Lab} = 20$ MeV indicate that there is no room for significant renormalization of the real part of the OP, under penalty of making the adjust of the data much worse.

Fig. 3 shows inelastic scattering angular distributions with excitation of the first excited state of ^{208}Pb (3^-, $E^* = 2.615$ MeV). Again, the dashed-dotted black and dashed red lines represent the results of the CCint and DWBAint approaches, respectively. The deformation lengths assumed in these calculations for the 3^- state are: $\delta_N = 0.865$ fm and $\delta_C = 0.797$ fm. The comparison between these theoretical cross sections (almost indistinguishable, except for $E_{\rm Lab} = 21$ MeV at backward angles) allows the estimation of the effect of the couplings, which is very small in this range of energies.

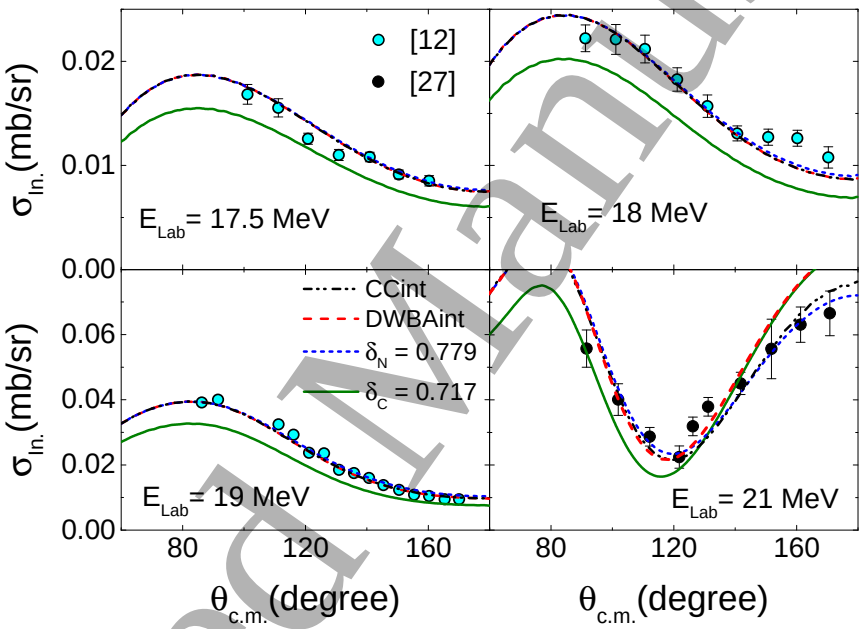

Figure 3. (color online) Experimental angular distributions for the excitation of the first 3^- $E^* = 2.615$ MeV ^{208}Pb state. The references where the data were obtained are indicated in the figure. The dashed-dotted black and dashed red lines represent the results of the CCint and DWBAint approaches, respectively. The dotted blue lines correspond to DWBAint calculations where the nuclear deformation value for this state was reduced by 10%. The solid green lines are the results of DWBAint, where now the Coulomb deformation value was reduced by 10%.

The dotted blue and solid green lines in Fig. 3 represent DWBAint calculations, in which the nuclear or the Coulomb deformation values for the 3^- state were reduced by 10% (*i.e.* $\delta_N = 0.779$ fm and $\delta_C = 0.797$ fm or $\delta_N = 0.865$ fm and $\delta_C = 0.717$ fm). Comparing these results with those obtained with $\delta_N = 0.865$ fm and $\delta_C = 0.797$ (dashed red lines), one can see that the effect of a variation of the nuclear deformation value on the cross sections is negligible, except for backward angles at $E_{\rm Lab} = 21$ MeV. On the other hand, the cross sections are quite sensitive to the Coulomb deformation. This behavior allowed us to obtain an accurate value for δ_C of this state. Since the error bars of the inelastic scattering data are known, we could also estimate the uncertainty: $\delta_C = (0.797 \pm 0.005)$ fm.

4.2. Energies around the barrier: $E_{\rm Lab} \leq 28$ MeV.

Fig. 4 shows excitation functions for the elastic scattering at (a) $\theta_{\rm cm} = 81.1^{\rm o}$ and $121^{\rm o}$ and (b) $\theta_{\rm cm} = 165.3^{\rm o}$. With the purpose of not overlapping the data, the cross sections for $\theta_{\rm cm} = 121^{\rm o}$ are displaced by a factor of 0.2. Note the change from linear (a) to logarithmic (b) scales. The dashed-dotted black and dashed red lines represent the results of the CCint and DWBAint approaches, respectively. The corresponding cross sections are almost indistinguishable up to about $E_{\rm Lab} = V_B = 21$ MeV. From this point forward, both approaches provide slightly different results, those from CCint describing precisely the experimental data. In particular, this behavior is also clearly observed in the region of the Coulomb rainbow, as indicated with an arrow in the figure.

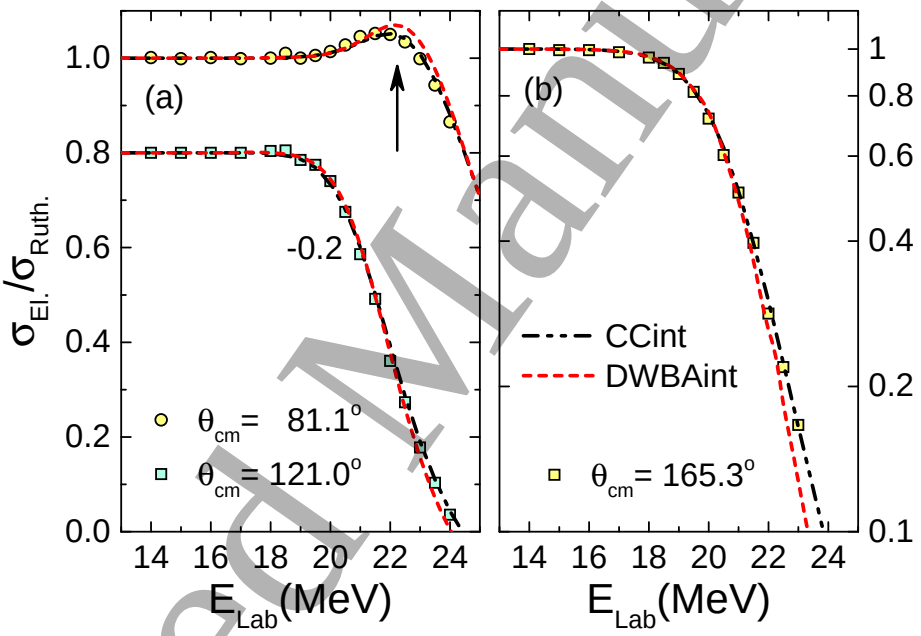

Figure 4. (color online) Excitation functions for the elastic scattering at three different angles indicated in the figure. The cross sections for $\theta_{\rm cm} = 121^{\rm o}$ are displaced by a factor of 0.2. The data were obtained in [13]. The dashed-dotted black and dashed red lines represent the results of the CCint and DWBAint approaches, respectively. Note the change from linear (a) to logarithmic (b) scales.

Fig. 5 presents experimental elastic scattering angular distributions at two different energies. Note the change from linear (a and b) to logarithmic (c and d) scales. For these energies, the CCint cross sections are in much better agreement with the data than those from DWBAint (see figure). This result is a clear indication of the importance of the couplings in this energy region. Even so, something else is still missing to describe the experimental angular distributions more accurately.

At this point we present results obtained within the DWBAsup and CCsup approaches. Both have one free parameter to fit the elastic scattering angular distribution, N_I, which is related to the strength of the superficial imaginary potential. In Fig. 6 we present the results of these theoretical calculations for $E_{\rm Lab} = 27.6$ MeV (the results for 23.6 MeV are similar). The agreement between data and theoretical

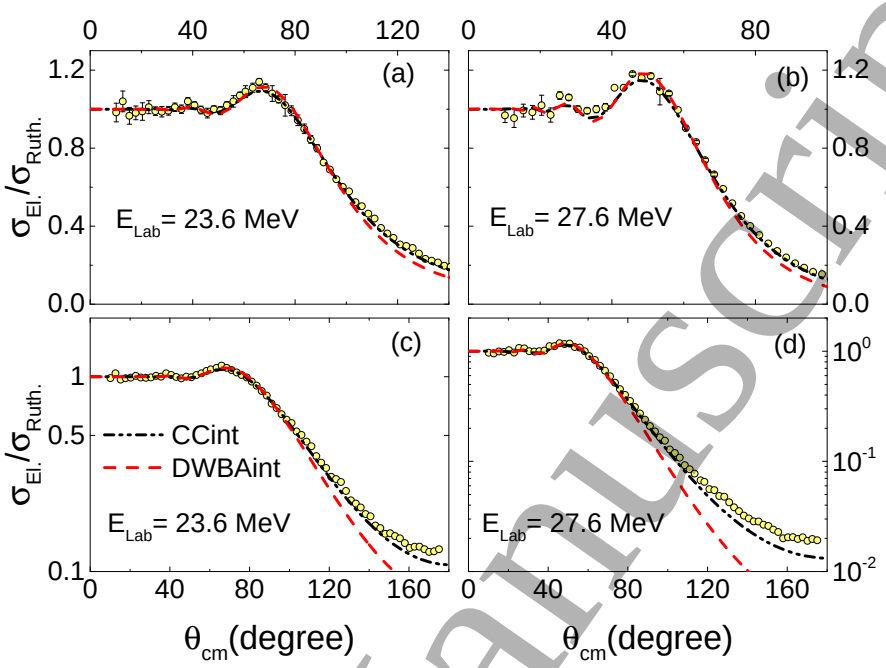

Figure 5. (color online) Experimental elastic scattering angular distributions in two different energies. The data were obtained from [16]. Note the change from linear (a and b) to logarithmic (c and d) scales. The lines represent the results of the CCint and DWBAint approaches.

cross sections improved (relative to CCint) at the backward angular region, as shown (in logarithmic scale) in panel (a) of the figure. In this region, the DWBAsup slightly underestimates the data for $\theta_{\rm cm} \geq 160^o$. In addition, important differences between DWBAsup and CCsup are shown (in linear scale) at the region of the Coulomb rainbow in panel (b). Thus, the best fit is clearly that provided by the CCsup approach.

Fig. 7 presents data for the excitation of the first 3^- state of ^{208}Pb at $E_{\rm Lab} = 23.5$ MeV. In order to test the sensitivity of the theoretical cross sections to the nuclear deformation value, we performed DWBAsup calculations with $\delta_N = \delta_W = 0.865$ fm and $\delta_N = \delta_W = 0.779$ (variation of 10%). Note, for these two theoretical results in Fig. 7, the high sensitivity of the cross sections at backward angles and the lack of sensitivity in the forward region.

As already mentioned, in this paper we also study the effect of including or excluding the imaginary part of the OP in the deformation related to the inelastic couplings. With this purpose, we also present, in Fig. 7, DWBAsup results in which was assumed $\delta_N = 0.865$ fm and $\delta_W = 0$. The effect of disconnecting the imaginary part is very large. From a theoretical point of view, it is not necessary that the δ_C and δ_N values are identical, but, as they are related to the deformation of the proton and matter densities of the same nucleus, one could expect similar values. Since we obtained, from sub-Coulomb analyses, $\delta_C = 0.797$ fm, it is expected for the nuclear deformation something about 0.8 fm. Deforming both (real and imaginary) with the same value, $\delta_N = \delta_W$, the data fit for the angular distribution presented in Fig. 7 in fact results in $\delta_N \approx 0.8$ fm.

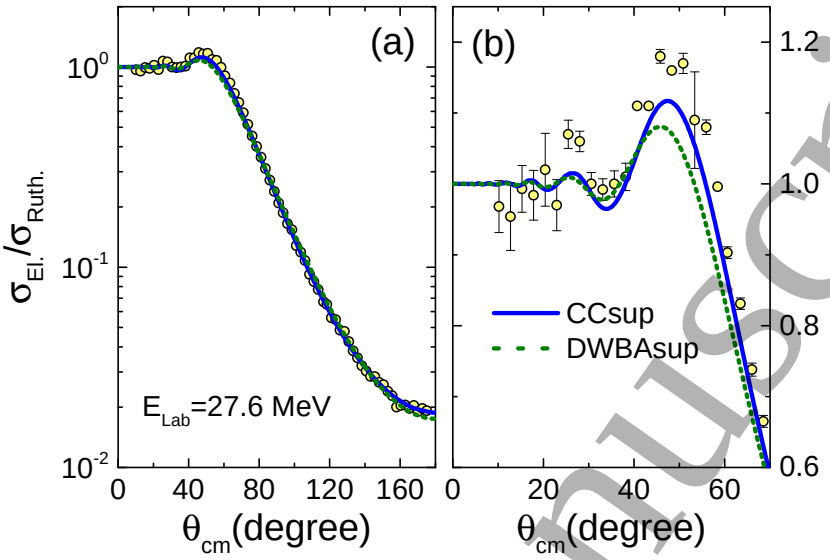

Figure 6. (color online) Experimental elastic scattering angular distribution for $E_{\rm Lab}$ = 27.6 MeV. Note the change from logarithmic (a) to linear (b) scales. The lines represent the results of the CCsup and DWBAsup approaches.

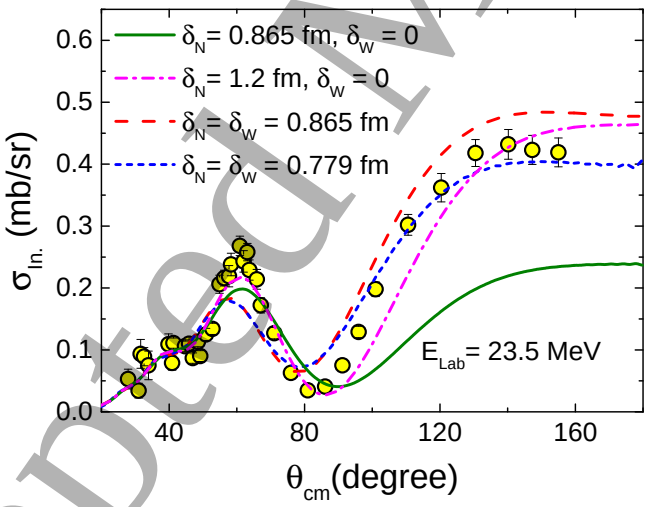

Figure 7. (color online) Experimental and theoretical angular distributions for the excitation of the 3^- E^* = 2.615 MeV state at $E_{\rm Lab}$ = 23.5 MeV. The data were obtained in [15]. The theoretical calculations were performed within the DWBAsup, with different values assumed for the nuclear deformation parameters δ_N and δ_W.

On the other hand, if $\delta_W = 0$ is assumed, the data fit provides $\delta_N \approx 1.2$ (see Fig. 7), a value much larger than that for δ_C. We consider this fact as an indication that the imaginary part of the OP should contribute for the deformation.

Fig. 8 also presents data for the excitation of the first 3^- state, but now for two bombarding energies. The lines in the figure represent the results of two different approaches: CCsup and DWBAsup. The theoretical angular distributions are in

reasonable agreement with the data. In these calculations, the nuclear deformation value was kept as $\delta_N = 0.865$ fm. Note the significant dependence of the cross sections on the model assumed in the calculations. For this reason, we estimate a larger uncertainty in the determination of the nuclear deformation value (in comparison with that of the Coulomb one): $\delta_N = (0.865 \pm 0.030)$ fm.

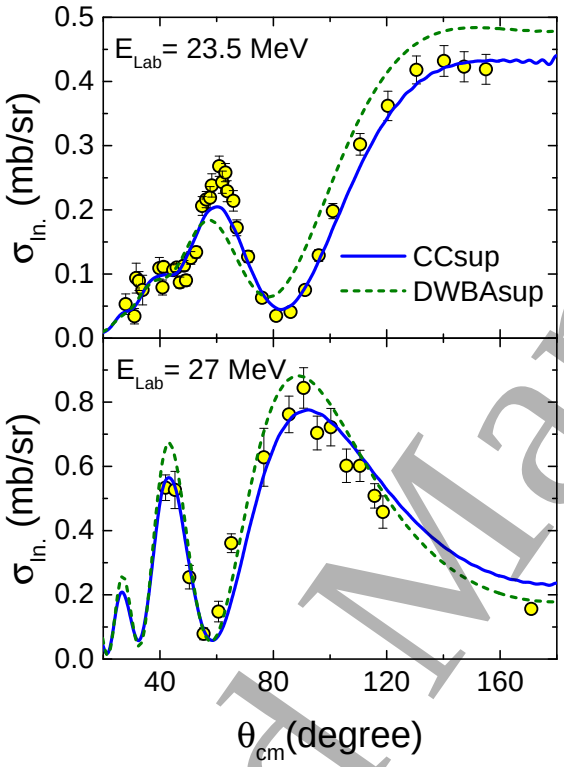

Figure 8. (color online) Experimental and theoretical angular distributions for the excitation of the first 3^- state at $E_{\rm Lab} = 23.5$ MeV and $E_{\rm Lab} = 27$ MeV. The data were obtained in [15,26]. The theoretical calculations were performed with $\delta_N = 0.865$ fm within different approaches: CCsup and DWBAsup.

Assuming eqs. (7) and (8), the set of 11 states presented in table 4 would be equivalent, to simulate theoretical elastic scattering cross sections, to that of the 111 states presented in table 2. Similar characteristic was successfully tested at $E_{\rm Lab} = 139$ MeV in [7]. Fig. 9 presents theoretical elastic scattering angular distributions for $E_{\rm Lab} = 27.6$ MeV, obtained within the CCint approach, assuming both sets of states. The figure also presents the results of DWBAint, just to emphasize the effect of the couplings. The CC theoretical elastic scattering angular distributions obtained with the sets of states of table 2 and table 4 are quite similar. We verified identical behavior for $E_{\rm Lab} = 23.6$ MeV as well as for much higher energies, within both: CCint and CCsup approaches. It is remarkable that a set with only 11 states of table 2 can simulate accurately the effect of the 111 states of table 2. This characteristics can be useful to facilitate numerical CC calculations in future works. However, the simulation does not work for sub-Coulomb energies, where the effect of the couplings of table 4 on the elastic scattering cross sections is significantly smaller than that of table 2.

Table 4. Excitation energy (in MeV), spin and nuclear length (in fm) values of 11 states that are equivalent (for the calculation of elastic scattering cross sections) to those of table 2.

S	0	1	2	3	4	5	6	7	8	9	10
E^*	13.7	17.3	8.74	7.35	7.71	4.93	8.37	5.51	5.29	5.55	4.90
δ_N	0.44	0.609	0.735	1.299	0.902	0.719	0.576	0.420	0.315	0.282	0.13

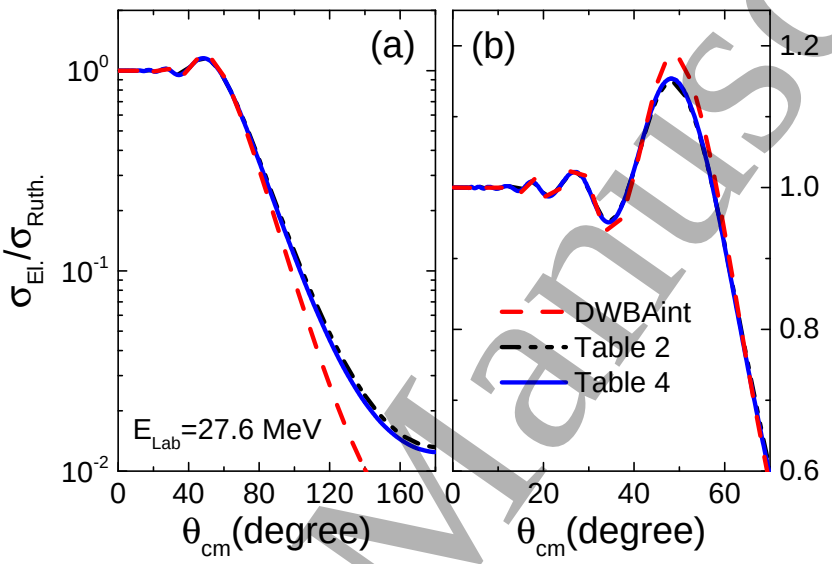

Figure 9. (color online) Theoretical elastic scattering angular distributions for $E_{\rm Lab}$ = 27.6 MeV within CCint assuming the sets of states presented in tables 2 and 4. For the purpose of comparison, the figure also shows the results obtained without considering the couplings (DWBAint).

The data analyses in the energy region around the barrier provided several important results. 1) There is not room for significant renormalization of the real part of the OP. 2) The values of the Coulomb and nuclear deformation parameters were accurately determined for the first 3^- ^{208}Pb state. 3) The CCsup approach resulted in the best elastic scattering data fits. 4) The imaginary part of the OP should be included in the deformation of the coupling potentials. 5) Eqs. (7) and (8) work very well in the simulation of the effect of the couplings on the elastic scattering cross sections. We proceed now with the data analyses for higher energies.

4.3. Energy region from $E_{\rm Lab}$ = 40 to 60 MeV.

We have found many data for inelastic excitation in this energy region, particularly in [29] where experimental angular distributions are provided for a large number of states with excitation energies up to about 6 MeV.

Fig. 10 presents an experimental elastic scattering angular distribution at $E_{\rm Lab}$ = 40.4 MeV. The results are shown in logarithmic, (a) and (c), and linear, (b) and (d), scales. Theoretical cross sections from CCint and DWBAint are shown in panels (a) and

(b). The CCint approach results in much better agreement with the data, indicating, again, the great importance of the inelastic couplings. Theoretical cross sections from DWBAsup and CCsup are shown in panels (c) and (d). The CCsup results are slightly better than those of the DWBAsup (see also the corresponding χ^2 values in table 3), and provides a good data description in the whole angular region.

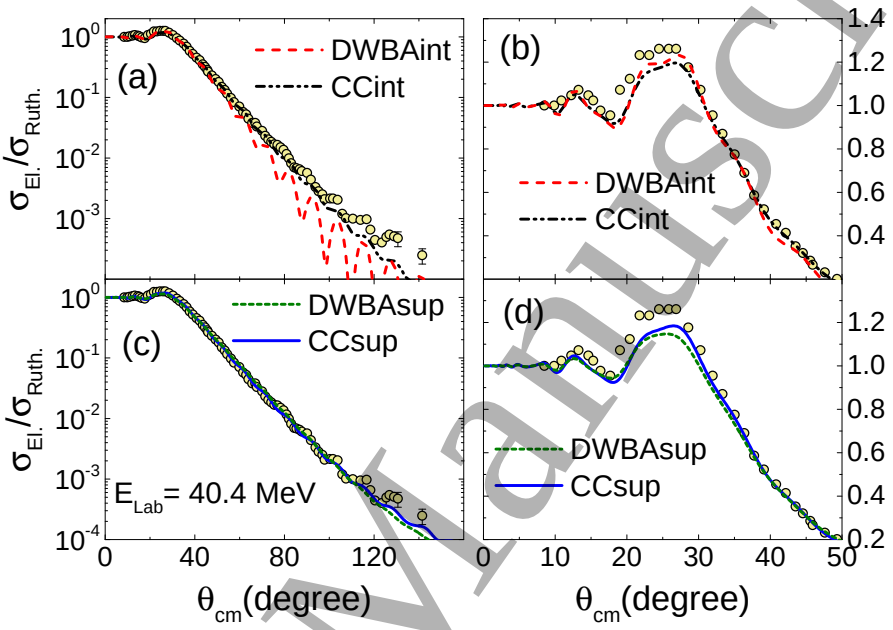

Figure 10. (color online) Experimental and theoretical angular distributions for the elastic scattering at $E_{\rm Lab} = 40.4$ MeV. The data were obtained in [29]. Note the change from logarithmic (panels (a) and (c)) to linear ((b) and (d)) scales.

Fig. 11 also presents elastic scattering angular distributions, but now for $E_{\rm Lab} = 50$ MeV. The inelastic couplings involved in the CCint result in damping of the strong oscillations (present in the cross sections from DWBAint), providing a better description of the data. The theoretical DWBAsup and CCsup angular distributions are almost identical and describe the data with precision resembling that of the CCint. In fact, for this distribution the N_I value of the CCsup approach is close to zero, indicating similar results of CCsup and CCint. Note, however, that the experimental cross sections for $E_{\rm Lab} = 50$ MeV are of order of 10^{-2} (ratio to Rutherford) at backward angles, while much smaller values, about 10^{-4}, were measured at $E_{\rm Lab} = 40.4$ MeV (see Fig. 10). Thus, probably the data analysis at 40.4 MeV is more sensitive to different theoretical approaches than that at 50 MeV.

Data and theoretical results for the elastic scattering at $E_{\rm Lab} = 58$ MeV are presented in Fig. 12. From this energy up, the DWBAint cross sections are much larger than the data at the backward angular region (see panel (a) of the figure). The couplings of the CCint improve the behavior of the theoretical results that now accompany the magnitude of the experimental cross sections, but with a stronger oscillatory pattern. The CCsup and DWBAsup angular distributions describe the data very well. This time the DWBAsup (instead of the CCsup) is the one that describes slightly better the

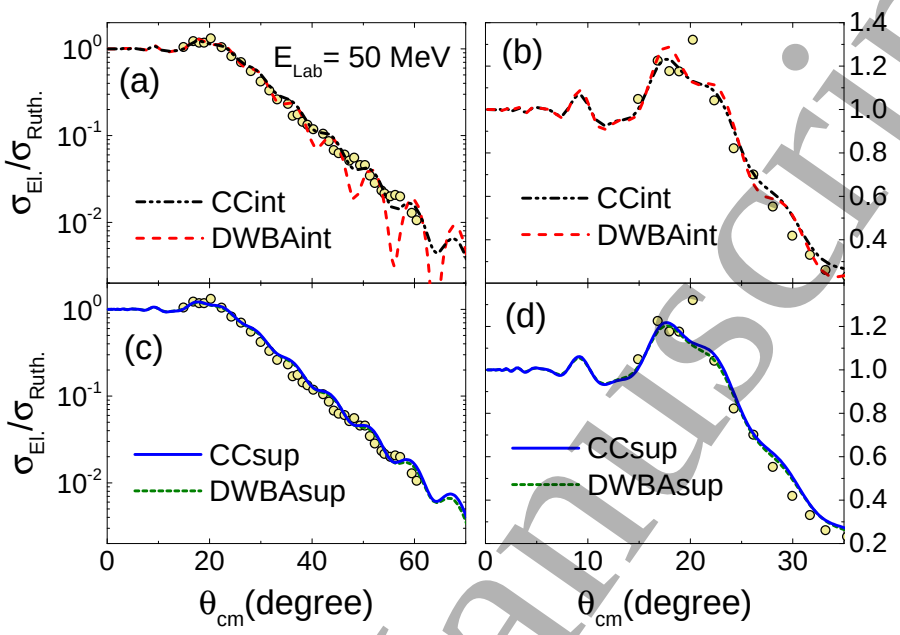

Figure 11. (color online) The same of Fig. 10, for $E_{\rm Lab}$ = 50 MeV. The data were obtained in [18].

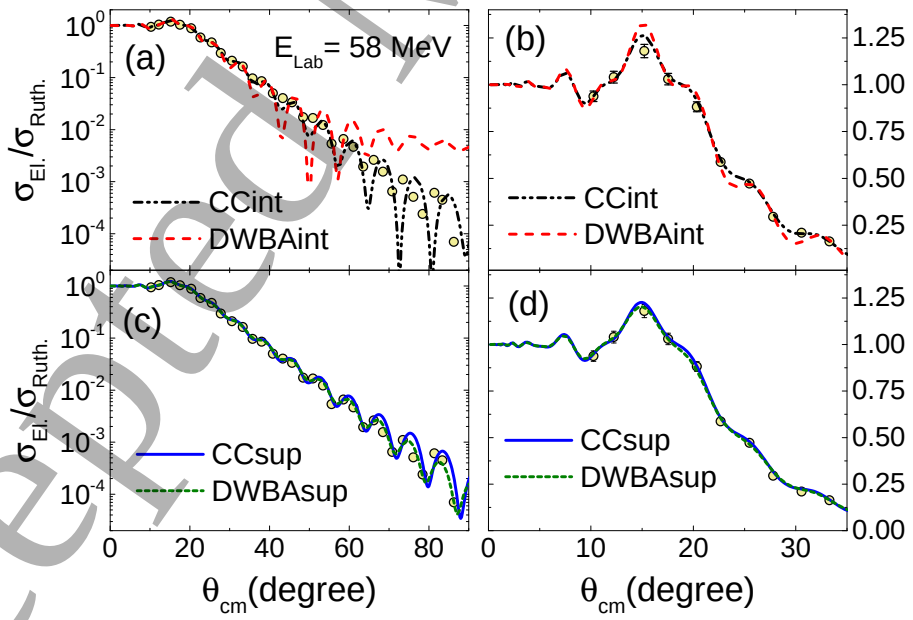

Figure 12. (color online) The same of Fig. 10, for $E_{\rm Lab}$ = 58 MeV. The data were obtained in [19].

oscillations of the data at backward angles (see panel (c)). This is an indication that other couplings besides those of table 2 become increasingly important for higher and higher energies.

In Fig. 13, we present an experimental angular distribution relative to the excitation

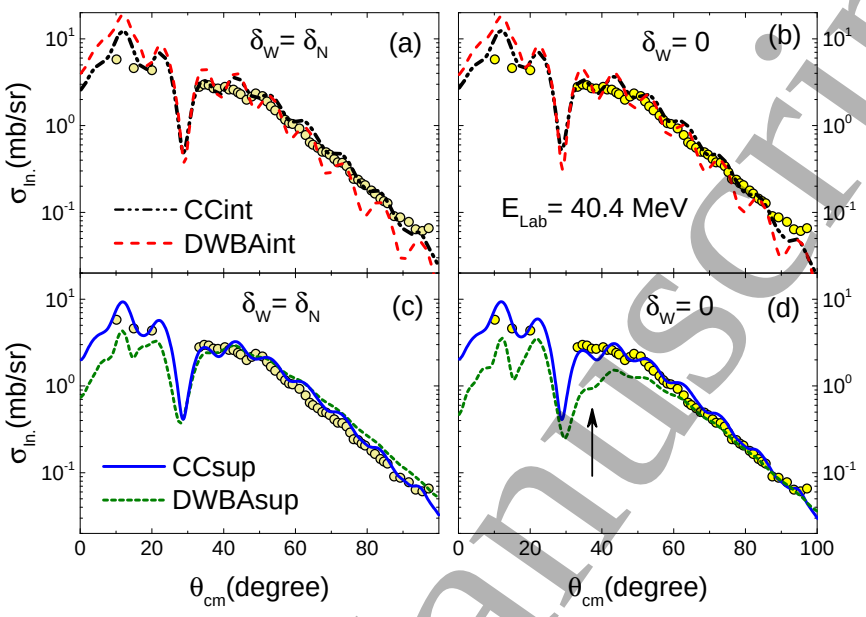

Figure 13. (color online) Angular distribution for the excitation of the first 3^- ^{208}Pb state at $E_{\rm Lab}$ = 40.4 MeV. The data were obtained in [29]. The lines represent the results of different approaches, in which $\delta_W = \delta_N$ or $\delta_W = 0$ were assumed.

of the first 3^- state of ^{208}Pb at $E_{\rm Lab}$ = 40.4 MeV. Panel (a) contains theoretical results from DWBAint and CCint. The inelastic couplings of CCint damp the oscillations (present in the DWBAint) approaching the theoretical cross sections to the data. Panel (c) shows slightly different results of the DWBAsup and CCsup approaches. The CCsup angular distribution describes the data slightly better than the other ones. This is the same behavior as that obtained for the elastic scattering at the same energy (see Fig. 10).

Panels (b) and (d) of Fig. 13 present theoretical distributions for the first 3^- state, but now assuming $\delta_W = 0$ (only) for this state. Almost identical theoretical results are found assuming $\delta_W = \delta_N$ or $\delta_W = 0$ in the cases of CCint and DWBAint (compare panels (a) and (b)). Thus, the deformation of the imaginary part of the OP is not important for the inelastic couplings when only the internal WS is included in this imaginary part. On the other hand, when a superficial contribution is added to the imaginary part, the $\delta_W = \delta_N$ and $\delta_W = 0$ assumptions provide significant differences in the theoretical results. For instance, compare the corresponding results of the DWBAsup in panels (c) and (d) of Fig. 13, in particular at the angular region indicated with an arrow in (d). In this case, the approach assuming $\delta_W = \delta_N$ results in much better agreement with the data than that with $\delta_W = 0$, indicating, again, that the deformation of the imaginary part of the OP should be included in the coupling potentials. For this energy, the N_I value of the CCsup is much smaller than that for DWBAsup (see table 3), and, therefore, the strength of the superficial imaginary potential for DWBAsup is much larger than that for CCsup. Consequently, the effect of deforming the imaginary part

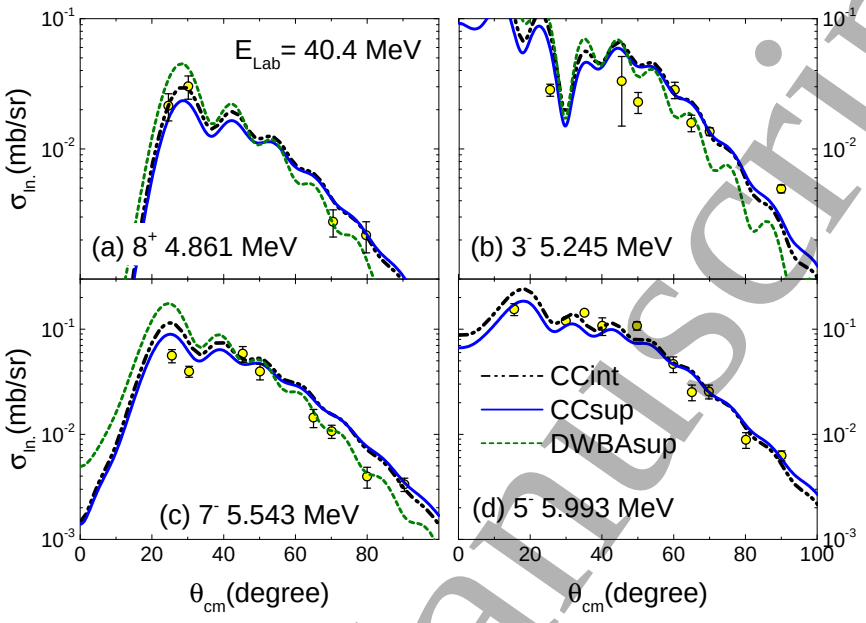

Figure 14. (color online) Angular distributions for the excitation of four ^{208}Pb states at $E_{\rm Lab}$ = 40.4 MeV. The spins and excitation energies of the states are indicated in the figure. The data were obtained from [29]. The lines represent the results of different theoretical approaches.

of the OP is much larger for DWBAsup than for CCsup (compare the results of panels (c) and (d)). Even so, in the case of CCsup the assumptions $\delta_W = \delta_N$ and $\delta_W = 0$ still result in slightly different angular distributions. All these results indicate that the deformation of the imaginary part of the OP is important, and should be assumed in CC calculations, but only in cases where this imaginary part has significant strength at the surface region. Of course, this is an expected result since the inelastic excitation is a peripheral reaction channel.

We present experimental and theoretical angular distributions for the inelastic excitation of four ^{208}Pb states at $E_{\rm Lab}$ = 40.4 MeV in Fig. 14. The deformation parameter values used in the respective calculations are those provided in table 2. The fit to the data presents some dependency on the model assumed in the calculations. The examples presented in this figure represent typical results obtained in our fits to the inelastic data in this energy region.

We present inelastic scattering angular distributions for 1^- states of different excitation energies in Fig. 15. The data were obtained at $E_{\rm Lab}$ = 40.4 and 48 MeV. The lines in the figure correspond to CCsup cross sections obtained assuming eq. (2) or eq. (6) to describe the 1^- coupling potentials. The theoretical results obtained with these two models are very similar in the angular region in which the data were obtained. The deformation lengths obtained through inelastic data fits with eq. (6) are presented in table 5. These values differ from those with eq. (2) (table 2) by a factor about 4. Thus, we conclude that the choice of assuming eq. (2) or eq. (6) to describe the couplings

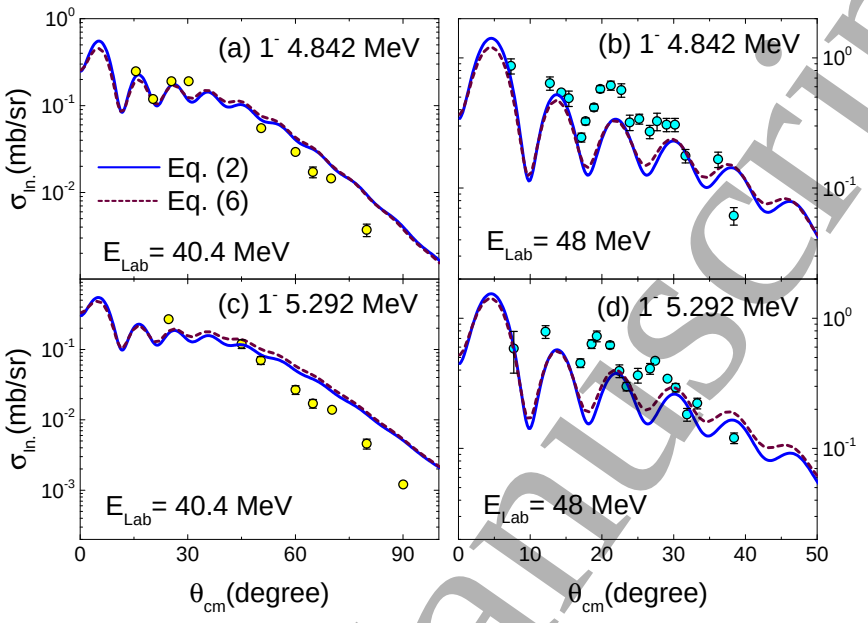

Figure 15. (color online) Angular distributions for the excitation of 1^- states at two different bombarding energies. The excitation and bombarding energies are indicated in the figure. The data were obtained from [29, 34]. The lines represent the results of the CCsup approach, assuming eqs. (2) or (6) to describe the 1^- coupling potentials.

of 1^- states is not important for the purpose of this work, as long as the respective different deformation length values are used in the theoretical calculations.

Table 5. Excitation energies, spins and deformation length values obtained through inelastic scattering data fits assuming eqs. (5) and (6) for the 0^+ and 1^- states, respectively.

E^* (MeV)	4.842	5.292	6.484	7.063	7.280	13.700	22.000
S	1	1	1	1	1	0	1
δ_N (fm)	0.035	0.041	0.066	0.039	0.023	0.390	0.143

4.4. Increasing the energy: $70 \leq E_{\rm Lab} \leq 80$ MeV.

Fig. 16 shows data and theoretical elastic scattering cross sections for $E_{\rm Lab} = 79.1$ MeV. The conclusions here are the same as those obtained for $E_{\rm Lab} = 58$ MeV: 1) the DWBAint cross sections are much larger than the data at the backward angular region; 2) the couplings of the CCint improve the agreement between data and theory, but differences remain in the oscillatory pattern; 3) the CCsup and DWBAsup approaches describe the data very well, but the DWBAsup describes slightly better the oscillations of the data at backward angles.

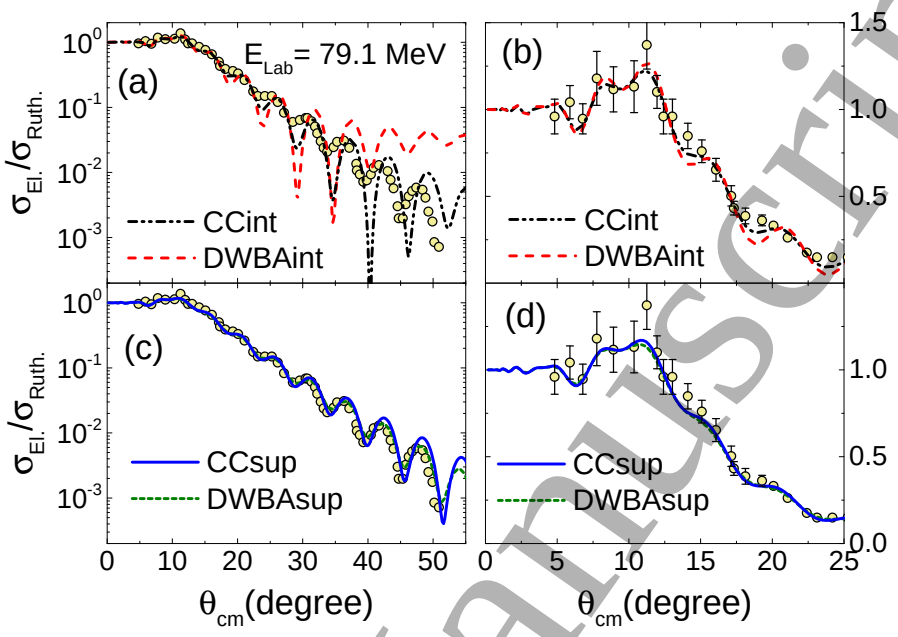

Figure 16. (color online) The same of Fig. 10, for $E_{\rm Lab} = 79.1$ MeV. The data were obtained in [20].

4.5. Intermediate energy region: $100 \leq E_{\rm Lab} \leq 172$ MeV.

Fig. 17 presents experimental and theoretical elastic scattering angular distributions for $E_{\rm Lab} = 104$ MeV (in (a) logarithmic and (c) linear scales), and for $E_{\rm Lab} = 120$ and 172 MeV (in logarithmic scale). Again, the DWBAint presents cross sections much larger than the data for rear angles. This time, the CCint also provides similar behavior, but for more backward angles compared to DWBAint. It seems that contributions of other couplings not included in table 2 become very important in this energy region. This contribution can be simulated through the inclusion of a superficial imaginary part in the OP, as can be observed in the DWBAsup and CCsup angular distributions shown in the figure, which agree well with the data. Coherently, the N_I values for CCsup are smaller than those for DWBAsup (see table 3).

Fig. 18 shows data and theoretical cross sections for the elastic scattering at $E_{\rm Lab} = 139$ MeV. The effect of the couplings included in the CCint causes a significant approximation of the theoretical elastic scattering cross sections to the data set compared to the result of DWBAint. Even so, the CCint angular distribution largely overestimate the data for $\theta_{cm} > 30^o$. The order of magnitude of the data is correctly reproduced by the DWBAsup and CCsup theoretical calculations (which are almost indistinguishable in the figure), but the beautiful nuclear rainbow of the experimental angular distribution around $\theta_{cm} = 70^o$ is not reproduced by the theoretical calculations. These data were adjusted very well in [23], assuming a WS shape for the real and imaginary parts of the OP (with six adjustable parameters). A shallow imaginary part was obtained ($W_0 \approx 23$ MeV), indicating a certain degree of "transparency" in the

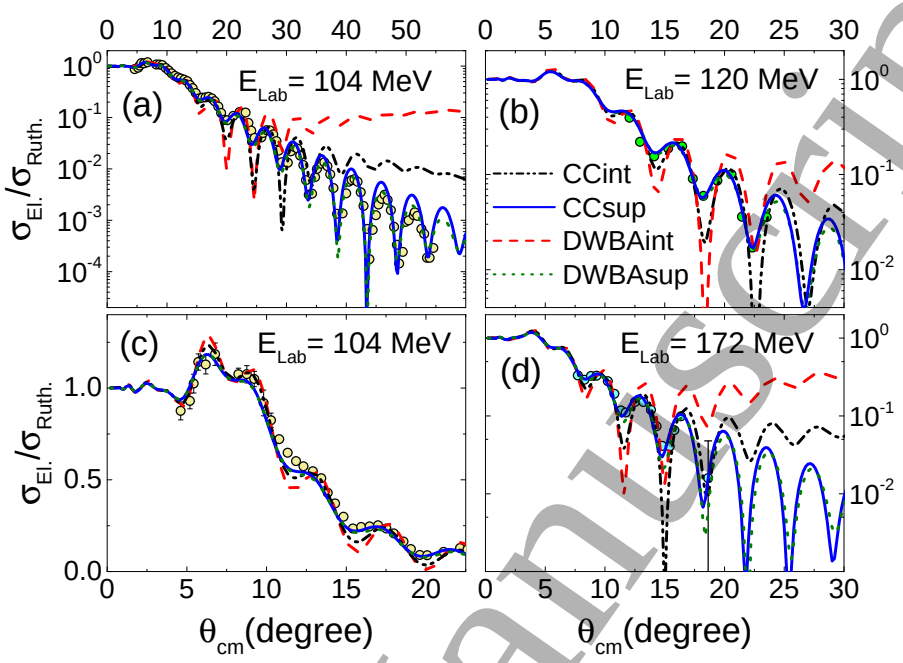

Figure 17. (color online) Elastic scattering angular distributions for $E_{\rm Lab}$ = 104 MeV, (a) in logarithmic and (c) linear scales, and for (b) 120 MeV and (d) 172 MeV, in logarithmic scale. The data were obtained from [21, 24, 38].

collision. We believe that a better adjust of this data set in the context of the present model would demand the inclusion of many other couplings (besides those of table 2) in the CC scheme, and the adjustment of the parameters of a shallow imaginary potential. This task is beyond the scope of the present work.

Fig. 19 presents data for the inelastic excitation of three ^{208}Pb states in different bombarding energies. All the theoretical angular distributions of the figure were obtained within the CCsup approach. In panel (a), the data correspond to the first 3^- state and the calculations were performed with and without deforming the imaginary part of the OP, *i.e.* assuming $\delta_W = \delta_N$ or $\delta_W = 0$ (only for the 3^- state). At this energy, $E_{\rm Lab}$ = 139 MeV, both options result in similar cross sections that differ each other by about 20%. Panel (c) corresponds to an 1^+ state with very high excitation energy. The theoretical calculations were performed considering eq. (2) or eq. (6) for the coupling potential. Small difference is observed between these two calculations, a similar behavior as that presented in Fig. 15 for other states and energies. Panels (b) and (d) of Fig. 19 refer to the 0^+ state with E^* = 13.7 MeV in two different energies. The calculations were performed assuming eq. (2) or eq. (5) for the coupling potential. Again no significant difference is observed in the corresponding angular distributions. Therefore, the use of eq. (2) or the alternative eqs. (5) and (6) result in similar cross sections, as long as different values for the corresponding deformation lengths are assumed in the calculations.

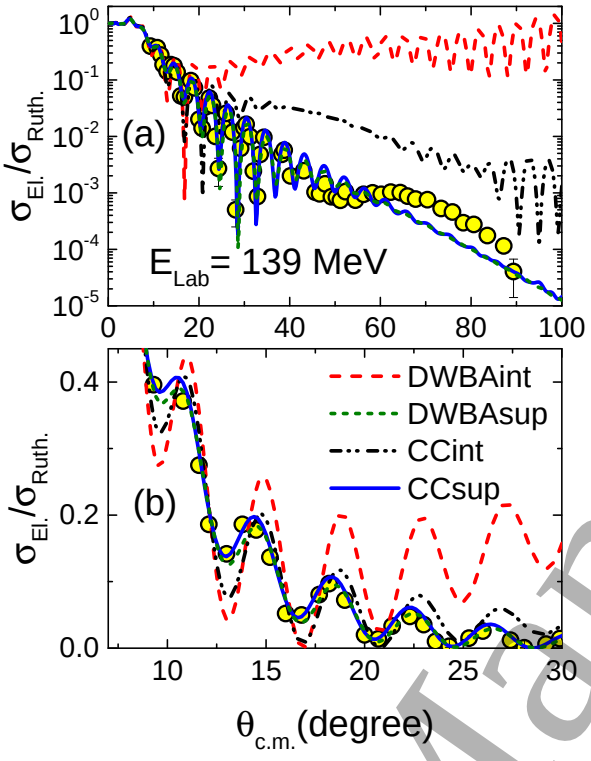

Figure 18. (color online) Elastic scattering angular distributions for $E_{\rm Lab}$ = 139 MeV, in (a) logarithmic and (b) linear scales. The data were obtained from [23].

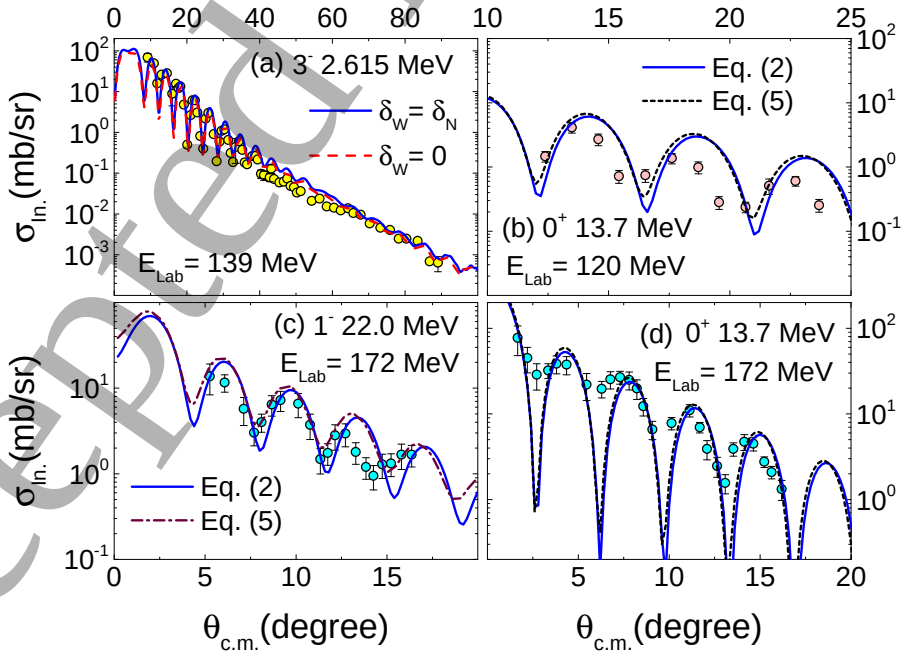

Figure 19. (color online) Inelastic scattering angular distributions for three ^{208}Pb excited states in different bombarding energies. The data were obtained from [23, 24, 38, 42, 43].

4.6. High energy region: $280 \leq E_{\rm Lab} \leq 700$ MeV.

As shown in Fig. 1, for high energies the N_I values obtained from data fits become much larger than those obtained in low energies. This is an indication that the absorption of flux by the peripheral reaction channels become quite important for high energies. Fig. 20 presents elastic scattering data and theoretical cross sections obtained within the DWBAsup and CCsup approaches. The adjustment for $E_{\rm Lab} = 288$ MeV is reasonable. However, for higher energies the theoretical distributions only follow the order of magnitude of the data but with a much larger oscillatory pattern. Indeed, the corresponding χ^2 values of table 3 are larger than 50%. Thus, we consider that the limits of application of the DWBAsup and CCsup theoretical models assumed in this work are found in this energy region.

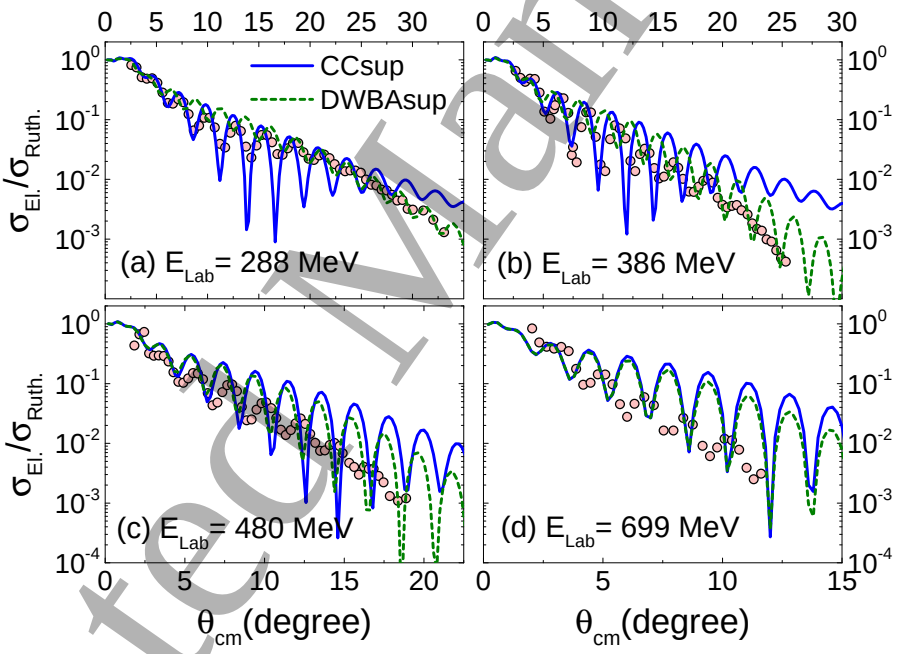

Figure 20. (color online) Experimental and theoretical elastic scattering angular distributions in the region of high energies. The data were obtained from [45, 46].

5. Discussion.

An observation of the figures presented so far shows that the CCint approach results in a quite reasonable agreement between theoretical and experimental elastic scattering angular distributions from sub-barrier energies up to $E_{\rm Lab} \approx 80$ MeV (about 4 times the Coulomb barrier height). Note that, within this approach, there is not any free parameter related to the OP to adjust the data, and only the internal WS shape is assumed for the imaginary part of the OP (simulating the fusion process). We thus consider that the data description within such condition in this wide energy region clearly demonstrates the great importance of the couplings presented in table

2. Nevertheless, the CCint approach fails in describing the data in the intermediate and high energy regions: $E_{\rm Lab} \geq 100$ MeV. In the intermediate one, the CCsup provides good data fits with N_I values significantly smaller than those obtained within the DWBAsup, again indicating the great importance of the inelastic couplings.

In order to study the importance of inelastic states with high excitation energies, we have done additional CC calculations assuming only the internal WS shape for the imaginary part of the OP (like in CCint), but now considering sets of states of different regions of excitation energy. The first region is composed just by the first 3^- state. The second region includes all states (of table 2) with excitation energies up to 5 MeV, while the third region involves states up to $E^* = 10$ MeV. The fourth region corresponds to all states of the table and, therefore, it is the result of the CCint as defined in the earlier sections. Of course, the calculations without any coupling, referred to as the DWBAint in the present paper, is also illustrative for this study.

Fig. 21 shows elastic scattering data and theoretical angular distributions for two bombarding energies. The theoretical calculations were performed according to the regions of excitation energies mentioned above. The effect of the low-lying 3^- $E^* = 2.615$ MeV on the elastic scattering cross sections is small. On the other hand, the effect increases a lot when states of high excitation energies are included in the couplings. Note that the difference of the CCint and the $E^* < 10$ MeV cross sections shown in the figure is due to the effect of only 7 states (see table 2). Even so, this difference is significant. We believe that the agreement between data and theoretical calculations could improve even more if other inelastic states (besides those of table 2) were included in the coupling scheme.

Of course, the states presented in table 2 represent just a fraction of the states that can be excited in the reaction ^{4}He + ^{208}Pb. At this point, it would be interesting to obtain a quantitative estimate of the "size"of this fraction. In order to address this question, self consistent Random Phase Approximation (RPA) calculations were performed for ^{208}Pb using the code `skyrme-rpa` [64]. The predicted strength functions were obtained by using the SLy5 interaction [65], which has also been adopted in several works to study the ^{208}Pb case (see *e.g.* [66, 67]). Before presenting the corresponding results, we discuss the sum rule for inelastic excitation.

The reduced transition probability for the inelastic excitation from the 0^+ ground-state (g.s.) to a particular state i (with spin S) is given approximately by [59]:

$$B(g.s. \rightarrow i; ES) \approx \left| \frac{3A\delta_i R_0^{S-1}}{4\pi} \right|^2 , \qquad (12)$$

where δ_i is the deformation length of state i and R_0 is the radius of the density of the nucleus. In fact, eq. (12) is a simplified version of eq. (4) when the density is considered as an uniform distribution without diffuseness. In this context, the energy-weighted sum rule (EWSR) is obtained by summing over all excited states (of a given spin S)

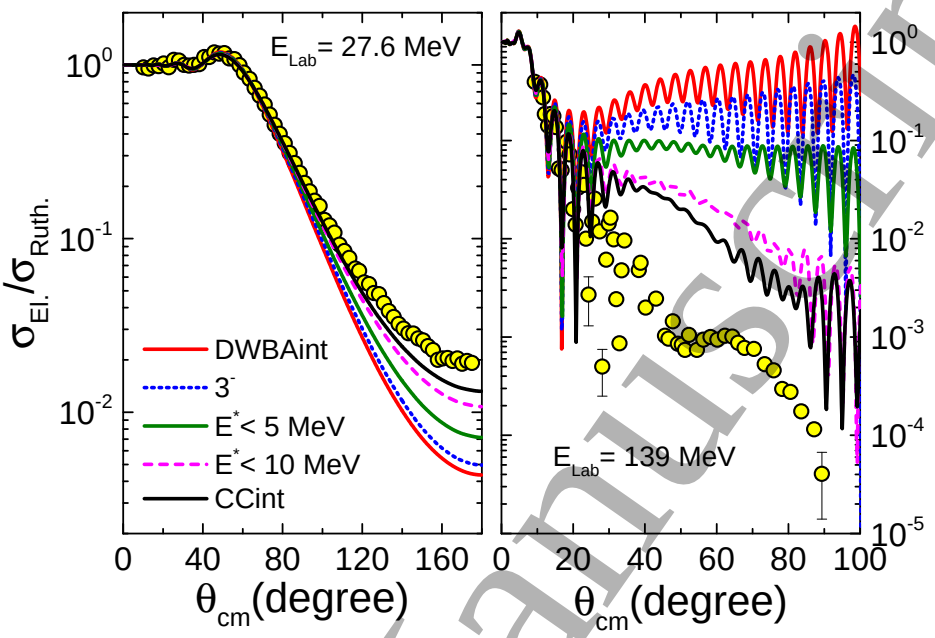

Figure 21. (color online) Experimental and theoretical elastic scattering angular distributions for two bombarding energies. The theoretical CC calculations were performed by coupling different sets of states corresponding to different regions of excitation energy.

and results in [59]:

$$\sum_i B(g.s. \rightarrow i; ES) \times E_i^* \approx \frac{3A\hbar^2}{8\pi m_0} S(2S+1) R_0^{2S-2}, \tag{13}$$

where E_i^* is the excitation energy of state i and m_0 is the mass of the nucleon. Combining eqs. (12) and (13), we obtain:

$$\sum_i E_i^* \, \delta_i^2 \approx \frac{2\pi\hbar^2}{3Am_0} S(2S+1), \tag{14}$$

that represents another form of writing the EWSR. Expressions (11) to (13) are not valid for $S = 0$ and 1 and should be appropriately modified (see *e.g.* [11]).

Table 6 presents the number of states (for each spin) and the corresponding fraction of the EWSR exhausted by the states of table 2. For $S = 0$, we have 165% of the EWSR with only one state (that with $E^* = 13.7$ MeV). However, it is well-known that the giant resonances contain contributions from many multipolarities that need to be disentangled from the angular distributions. Experimental results using a multipole decomposition analysis show that the exhausted EWSR at this excitation energy is about 40% [68]. Thus, the states of table 2 exhausts about 100% of the EWSR for $S = 0$, 1, 2 and 3. On the other hand, for higher spins the states presented in table 2 exhausts only a quite small fraction of the EWSR, indicating that there is still room for including many ^{208}Pb states (and also those of ^{4}He) in the CC calculations.

Table 6. Number of states and fraction of the EWSR exhausted by the states of table 2 for each spin S. The table also presents the average excitation energy (in MeV and for each spin) obtained for the states of table 2 and from the RPA calculations.

S	0	1	2	3	4	5	6	7	8	9	10
number	1	6	12	33	21	15	6	8	4	4	1
% EWSR	165	95	112	140	41	11	8.5	2.2	0.9	0.6	0.1
$\langle E^* \rangle$ Table	13.7	17.3	8.7	7.3	7.7	4.9	8.4	5.5	5.3	5.5	4.9
$\langle E^* \rangle$ RPA	14.1	20.0	10.0	9.0	15.2	17.3	21.7	24.9	26.1	26.1	

We turn now to the results of our RPA calculations. Table 6 contains the average excitation energy values (for each spin) obtained with the states of table 2 and from the RPA calculations. For each spin, these average values are defined according to eqs. (15) and (16), for table 2 and RPA respectively. For spins 0, 1, 2 and 3 the average values for the states considered in our CC calculations are similar to those obtained from RPA. This is consistent with the other result, already commented, that the states of table 2 exhaust about 100% of the EWSR for $0 \leq S \leq 3$. On the other hand, for $S \geq 4$ the states included in the CC calculations exhaust only a small fraction of the EWSR and, as presented in table 6, the average excitation values for the CC states are much smaller than those from RPA. This is an indication that many states of high spins and large excitation energies could provide important contribution if were included in the CC calculations.

$$\langle E^* \rangle = \frac{\sum E_i^* \, \delta_i^2}{\sum \delta_i^2}, \tag{15}$$

$$\langle E^* \rangle = \frac{\sum E_i^* \, B(g.s. \rightarrow i; E\lambda)}{\sum B(g.s. \rightarrow i; E\lambda)}. \tag{16}$$

Fig. 22 presents the fraction of the EWSR reached up to a particular state i (summation for all states from the g.s. to the state i) as a function of the excitation energy of this state i, for some spin values. The data presented in this figure correspond to the states of table 2 and to the RPA calculations. For $S = 2$, the states included in the CC calculations present similar behavior as those from RPA. In this case, note the presence of a state with excitation energy of about 10 MeV that exhausts a large fraction of the EWSR. For $S = 3$, the RPA calculations overpredict the importance of the first 3^- state. The strong contribution of a state around 20 MeV (included in the CC calculations) is not present in the RPA. For higher spins, the behavior of the states of table 2 is similar to that of the RPA calculations for low excitation energies. It is clear, however, that many states with $E^* > 7$ MeV should be included in the CC calculations.

Finally, we test our model in the description of the fusion at sub-barrier energies. In this energy region, the major process related to fusion is the evaporation of one neutron after the formation of the compound nucleus. Data for this process (from [69]) as a function of the difference between the energy (center of mass) and the barrier height

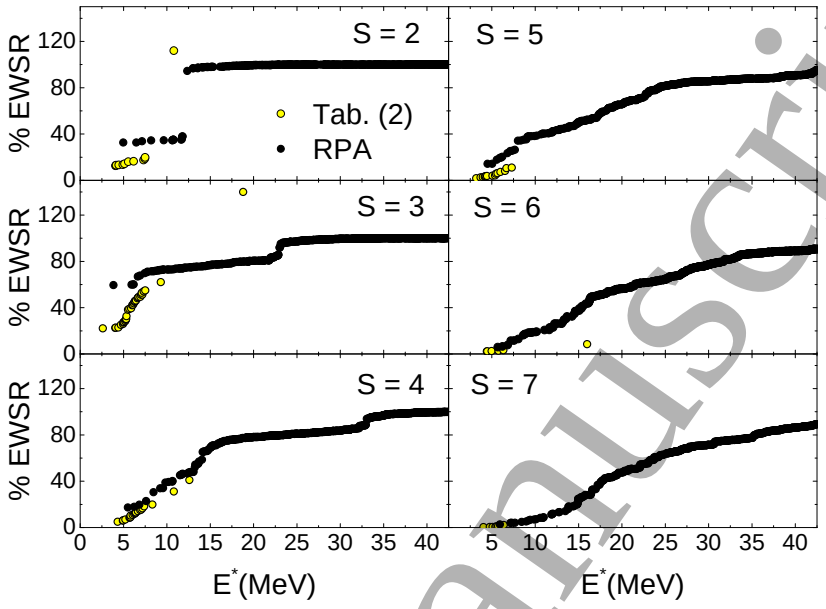

Figure 22. (color online) Fraction of the EWSR reached up to a particular state i as a function of the excitation energy of this state, for some spin values. The data correspond to the states of table 2 and to the RPA calculations.

are presented in fig. 23. The figure also shows the theoretical fusion cross sections for the CCint and DWBAint approaches. The effect of the couplings is small and both theoretical results describe the data accurately up to the region near the barrier (where other processes should contribute to the fusion).

6. Conclusion

In this work, we have assumed the recently proposed BNP interaction for the real part of the OP, which is not dependent on the energy. The purpose was to determine the energy region in which a good data description is possible to be obtained in this condition. We have taken into account the effect of couplings to 111 ^{208}Pb excited states. The CC calculations performed in this work are realistic in the sense that the deformation length values associated to the coupling potentials were obtained from the corresponding inelastic scattering data fits.

The CCint approach does not contain free parameters related to the OP, whose imaginary part involves only internal absorption to simulate fusion. Within this approach, we obtained a quite reasonable description of the elastic scattering data set from sub-barrier energies to about $E_{\rm Lab} = 80$ MeV. A good data description is obtained also in the intermediate energy region, $100 \leq E_{\rm Lab} \leq 172$ MeV, but in this case it was necessary to include a superficial contribution in the imaginary part of the OP through the CCsup approach. Consistently, the N_I values obtained within CCsup are

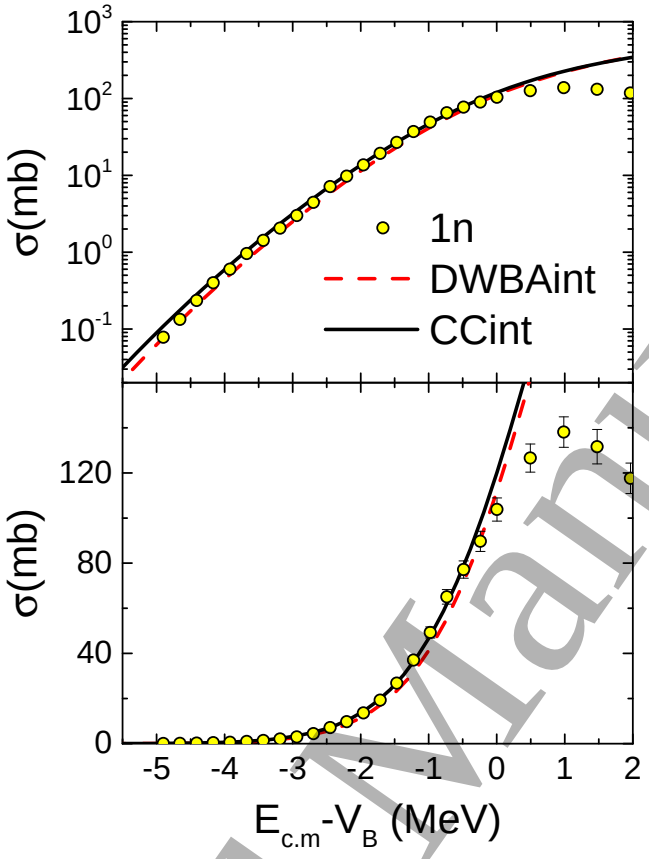

Figure 23. (color online) Data (from ref. [69]) for the evaporation of one neutron from the compound nucleus as a function of the difference of the energy relative to the barrier height. The figure also shows the theoretical predictions for the fusion cross sections within the CCint and DWBAint approaches. Note the change from logarithmic (top) to linear (bottom) scale.

considerably smaller than those obtained with the DWBAsup. The adjust of the data at the high energy region was poor for both approaches: DWBAsup and CCsup. This establishes the limit of the present models.

Our analyses provided other important conclusions. 1) The imaginary part of the OP should be included in the deformation of the coupling potentials. 2) Eqs. (7) and (8) work well in the simulation of the effect of the couplings of table 2 on the elastic scattering cross sections, except in the sub-barrier energy region. 3) The use of eq. (2) or the alternative eqs. (5) and (6) for the coupling potentials relative to the spins $S = 0$ and 1 result in similar cross sections, as long as different values for the corresponding deformation lengths are assumed in the calculations.

There is room to improve the scope of the present theoretical model through the inclusion of other couplings in the CC calculations. The states considered in the present work represent only a small fraction of the EWSR for high spins. This is an indication

that important contributions can be related to states with spins $S \geq 4$ and excitation energies $E^* \geq 7$ MeV. Furthermore, contribution of other reaction channels as, for instance, to transfer reactions can also be important for the elastic scattering process.

Acknowledgments

This work was partially supported by Fundação de Amparo à Pesquisa do Estado de São Paulo (FAPESP, Brazil) Proc. Nos. 2018/04965-4, 2018/09998-8, 2019/07767-1 and 2019/05769-7; by Conselho Nacional de Desenvolvimento Científico e Tecnológico (CNPq, Brazil) Proc. Nos. 302160/2018-3 and 304056/2019-7; and by project INCT-FNA Proc. No. 464898/2014-5.

References

[1] Satchler G R 1991 *Phys. Rep.* **199** 147.
[2] Brandan M E and Satchler G R 1997 *Phys. Rep.* **285** 143.
[3] Kobos A M, Brown B A, Hodgson P E, Satchler G R and Budzanowski A 1982 *Nucl. Phys. A* **384** 65.
[4] Chamon L C, Carlson B V, Gasques L R, Pereira D, de Conti C, Alvarez M A G, Hussein M S, Cândido Ribeiro M A, Rossi E S Jr. and Silva C P 2002 *Phys. Rev. C* **66** 014610.
[5] Chamon L C, Gasques L R, Nobre G A P, Rossi Jr E S, deBoer R J, Seymour C, Wiescher M and Kiss G G 2015 *J. Phys. G* **42** 055102.
[6] Chamon L C and Gasques L R 2016 *J. Phys. G* **43** 015107.
[7] Chamon L C, Gasques L R and Zamora J C 2020 *J. Phys. G* **47** 105103.
[8] Chamon L C, Carlson B V and Gasques L R 2021 *Comput. Phys. Comm* **267** 108061.
[9] Chamon L C, Gasques L R and Carlson B V 2011 *Phys. Review C* **84** 044610.
[10] Chamon L C, Gasques L R, Alves L F M, Guimarães V, Descouvemont P, deBoer R J and Wiescher M 2014 *J. Phys. G* **41** 035101.
[11] Harakeh M N and van der Woude M 2001 *Giant Ressonances: Fundamental High-Frequency Modes of Nuclear Excitation*, Oxford University Press, New York.
[12] Chamon L C and Morales Botero D F 2018 *J. Phys. G* **45** 029502.
[13] Goldring G, Samuel M, Watson B A, Bertin M C and Tabor S L 1970 *Phys. Lett. B* **32** 465.
[14] Barnett A R and Phillips W R 1969 *Phys. Rev.* **186** 1205.
[15] Lilley J S, Franey M A and Feng D H 1980 *Nucl. Phys. A* **342** 165.
[16] Karcz W, Kluska I, Sanok Z, Szmider J, Szymakowski J, Wiktor S and Wolski R 1972 *Acta Phys. Pol. B* **3** 525.
[17] C.Basu *et al* 2012 *AIP Conf. proc.* **1491** 321.
[18] David P, Debrus J, Essen H, Luebke F, Mommsen H, Schoenmackers R, Soyez W, Geramb H V V and Hefter E F 1976 *Z. Phys. A* **278** 281.
[19] Tickle R and Gray W S 1975 *Nucl. Phys. A* **247** 187.
[20] Rutledge Jr. L L and Hiebert J. C. 1976 *Phys. Rev. C* **13** 1072.
[21] Hauser G, Löhken R, Rebel H, Schatz G, Schweimer G W and Specht J 1969 *Nucl. Phys. A* **128** 81.
[22] Kurihara T, Kubono S, Sekiguchi M, Tanaka M H, Sakai M, Fujita Y, Fujiwara M and Gerlic E 1986 *Nucl. Phys. A* **457** 45.
[23] Goldberg D A, Smith S M, Pugh H G, Roos P G and Wall N S 1973 *Phys. Rev. C* **7** 1938.
[24] Morsch H P, Sukosd C, Rogge M, Turek P, Machner H and Mayer-Boricke C 1980 *Phys. Rev. C* **22** 489.
[25] Barnett A R, Feng D H and Goldfarb U B 1974 *Phys. Lett. B* **48** 290.

[26] Baxter A M, Hinds S, Spear R H, Zabel T H and Smith R 1981 *Nucl. Phys. A* **369** 25.
[27] Valnion B D, Oelmaier I W, Hofer D, Zanotti-Miiller E, Graw G, Atzrott U, Hoyler F and Staudt G 1994 *Z. Phys. A* **350** 11.
[28] Valnion B D, Ponomarev V Yu, Eisermann Y, Gollwitzer A, Hertenberger R, Metz A, Schiemenz P and Graw G 2001 *Phys. Rev. C* **63** 024318.
[29] Atzrott U 1995 *Ph.D. thesis* Universität Tübingen, Tübingen.
[30] Heusler A, Jolos R V, Faestermann T, Hertenberger R, Wirth H -F and von Brentano P 2016 *Phys. Rev. C* **93** 054321.
[31] Alster J 1966 Phys. Rev. **141** 1138.
[32] Satchler G R, Broek H W and Yntema J L 1965 *Phys. Lett.* **16** 52.
[33] Baker F T and Tickle R 1970 *Phys. Lett. B* **32** 47.
[34] Decowsk P, Morsch H P and Benenson W 1981 *Phys. Lett. B* **101** 147.
[35] Fujita Y, Shimoda T, Miyatake H, Takahashi N, Fujiwara M, Morinobu S, Yamagata T, Takamatsu J, Terakawa A and Folger H 1992 *Phys. Rev. C* **45** 993.
[36] Yamagata T, Kishimoto S, Yuasa K, Saeki B, Iwamoto K, Tanaka M, Fukuda T, Miura I, Inoue M and Ogata H 1982 *Nucl. Phys. A* **381** 277.
[37] Youngblood D H, Rozsa C M, Moss J M, Brown D R and Bronson J D 1977 *Phys. Rev. Lett.* **39** 1188.
[38] Harakeh M N, van Heyst B, van der Borg K and van der Woude A 1979 *Nucl. Phys. A* **327** 373.
[39] Poelhekken T D, Hesmondhalgh S K B, Hofmann H J, van der Woude A and Harakeh M N 1992 *Phys. Lett. B* **278** 423.
[40] Youngblood D H, Bogucki P, Bronson J D, Garg U, Lui Y -W, and Rozsa C M 1981 *Phys. Rev. C* **23** 1997.
[41] Bertrand F E, Satchler G R, Horen D J, Wu J R, Bacher A D, Emery G T, Jones W P, Miller D W and van der Woude A 1980 *Phys. Rev. C* **22** 1832.
[42] Morsch H P, Decowski P, Rogge M, Turek P, Zemlo L, Martin S A, Berg G P A, Hurlimann W, Meissburger J and Romer J G M 1983 *Phys. Rev. C* **28** 1947.
[43] Morsch H P *et al* 1982 Phys. Lett. B **119** 311.
[44] Barnett A R and Lilley J S 1974 Phys. Rev. C **9** 2010.
[45] Bonin B *et al* 1984 *Nucl. Phys. A* **430** 349, and 1985 *Nucl. Phys A* **445** 381.
[46] Uchida M *et al* 2004 *Phys. Rev. C* **69** 051301.
[47] Wagner W T, Crawley G M, Hammerstein G R and McManus H 1975 *Phys. Rev. C* **12** 757.
[48] Lewis M B, Bertrand F E and Fulmer C B 1973 *Phys. Rev. C* **7** 1966.
[49] Fujita Y, Fujiwara M, Morinobu S, Katayama I, Yamazaki T, Itahashi T, Ikegami H, and Hayakawa S I 1989 *Phys. Rev. C* **40** 1595.
[50] Fujita Y, Fujiwara M, Morinobu S, Katayama I, Yamazaki T, Itahashi T, Ikegami H, and Hayakawa S I 1985 *Phys. Rev. C* **32** 425.
[51] Hintz N M *et al* 1988 *Phys. Rev. C* **37** 692.
[52] Poltoratska I *et al* 2012 *Phys. Rev. C* **85** 041304(R).
[53] Adams G S, Bacher A D, Emery G T, Jones W P, Miller D W, Love W G and Petrovich F 1980 *Phys. Lett. B* **91** 23.
[54] McDaniels D K *et al* 1987 Nucl. Phys. A **467** 557.
[55] Scott A, Mathur N P and Petrovich F 1977 *Nucl. Phys. A* **285** 222.
[56] Morsch H P, Decowski P and Benenson W 1978 *Nucl. Phys. A* **297** 317.
[57] Del Vecchio R M, Freedman S J, Garvey G T and Oothoudt M A 1975 *Phys. Rev. Lett.* **34** 1296.
[58] Del Vecchio R M, Freedman S J, Garvey G T and Oothoudt M A 1976 *Phys. Rev. C* **13** 2089(R).
[59] Satchler G R, 1983 *Direct Nuclear Reactions*, Oxford University Press, New York, p. 616.
[60] Zagatto V A B *et al* 2018 *Phys. Rev. C* **97** 054608.
[61] Yagi K *et al* 1964 *Phys. Lett.* **10** 186.
[62] Dickens J K, Perey F G and Satchler G R 1965 *Nucl. Phys.* **73** 529.
[63] Experimental Nuclear Reaction Data (EXFOR), https://www-ndf.iaea.org/exfor/.

[64] Coló G, Cao L, Nguyen V G and Capelli L 2013 *Comp. Phys. Comm.* **184** 142.
[65] Chabanat E, Bonche P, Haensel P, Meyer J and Schaeffer R 1998 *Nucl. Phys. A* **635** 231.
[66] Cuong D C, Khoa T D and Colò G 2010 *Nucl. Phys. A* **836** 11.
[67] Cao L, Sagawa H and Colò G 2012 *Phys. Rev. C* **86** 054313.
[68] Youngblood D H, Lui Y W, Clark H L, John B, Tokimoto Y and Chen X 2004 *Phys. Rev. C* **69** 034315.
[69] Barnett A R and Lilley J S 1974 *Phys. Rev. C* **9** 2010.